Electrochemistry of Redox-Active Molecules Confined within Narrow Carbon Nanotubes

Jack W. Jordan,[a] William J. V. Townsend,[b] Lee R. Johnson,[a,b] Darren. A. Walsh,[a,b] Graham N. Newton,[a,b] Andrei N. Khlobystov[c]*

a - GSK Carbon Neutral Laboratories for Sustainable Chemistry, University of Nottingham, Nottingham, NG7 2TU, UK

b - The Faraday Institution, Quad One, Harwell Science and Innovation Campus, Didcot, UK

c - School of Chemistry, University of Nottingham, Nottingham, NG7 2RD, UK

*andrei.khlobystov@nottingham.ac.uk

Abstract

Confinement of molecules within nanocontainers can be a powerful tool for controlling the states of guest-molecules, tuning properties of host-nanocontainers and triggering the emergence of synergistic properties within the host-guest systems. Among nanocontainers, single-walled carbon nanotubes – atomically thin cylinders of carbon, with typical diameters below 2 nm and lengths reaching macroscopic dimensions – are ideal hosts for a variety of materials, including inorganic crystals, and organic, inorganic and organometallic molecules. The extremely high aspect ratio of carbon nanotubes is complemented by their functional characteristics, such as exceptionally high electrical conductivity and thermal, chemical and electrochemical stability, making carbon nanotubes ideal connectors between guest-molecules and macroscopic electrodes. The idea of harnessing nanotubes both as nanocontainers and nanoelectrodes has led to the incorporation of redox-active species entrapped within nanotube cavities where the host-nanotubes may serve as conduits of electrons to/from the guest-molecules, whilst restricting the molecular positions, orientations, and local environment around the redox centres. This review gives a contemporary overview of the status of molecular redox chemistry within ultra-narrow carbon nanotubes (nanotubes with diameters approaching molecular dimensions) highlighting the opportunities, pitfalls, and gaps in understanding of electrochemistry in confinement, including the role of nanotube diameter, size and shape of guest-molecules, type of electrolyte, solvent and other experimental conditions.

Keywords: carbon nanotubes; redox reactions; electrochemistry; electrocatalysis; energy storage materials.

Introduction

Due to their high electrical conductivity, low densities and high surface areas carbon nanotubes (CNTs) have often been used as additives to connect otherwise insulating materials to electrodes or current

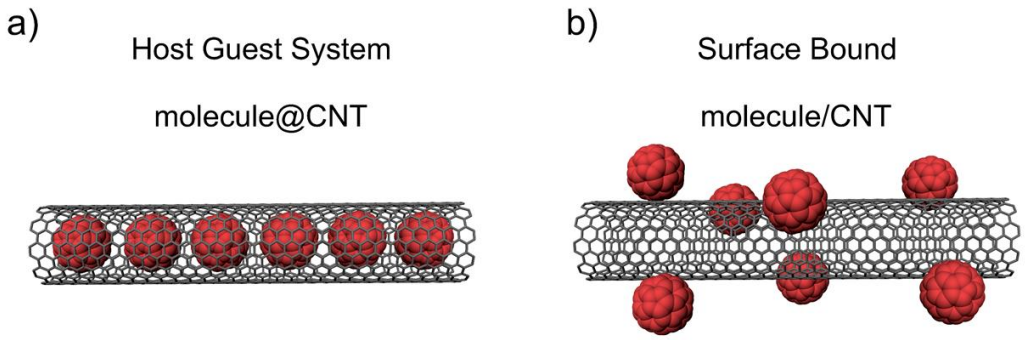

Figure 1. Schematic diagrams of molecules (C_{60} fullerenes used as an example) (a) encapsulated in or (b) adsorbed on single-walled carbon nanotubes.

collectors,[1] thus mediating electron transfer between redox active species and the rest of the electrochemical cell. This is normally achieved by loading the active species onto the exterior surface of the CNT (Figure 1a). However, CNTs also possess an internal cavity in which guest species can be entrapped.[2] Confinement of molecular species and materials to nanoscale dimensions, either within a cavity, pore, pocket, channel or between sheets of a layered material can significantly alter their chemical and physical properties.[3] Confinement of molecular species within CNTs can increase catalytic activity, improve the cyclability of catalysts and control reaction selectivity due to effects emerging in nanoscale volumes.[4] Confinement can also enhance the electronic properties of both the CNT and guest- species through guest-guest or host-guest charge transfer interactions.[5] The effect of confinement on electrochemical processes is only now beginning to be fully explored,[6-8] due to the complexity of the different competing effects and interactions influencing the reactivity in these exotic environments. For CNTs in particular, the need for methods that can reliably encapsulate molecules within CNT cavities (symbol @ indicates encapsulation of guest-molecules) rather than adsorb them onto the nanotube surface (designated as molecule/CNT; Figure 1b)[9] has also hindered research in this area. Additionally, the specific characteristics of a batch of SWCNTs are significantly impacted by the synthetic methods used in their preparation. Nanotube growth methods, such as arc-discharge, laser ablation and chemical vapour deposition (CVD), all produce SWCNTs with varying diameters and differing levels of chiral purity and defects. Development of alternative methods, such as the high-pressure carbon monoxide (HiPCO)

nanotube synthesis, has been employed to improve diameter and chirality selectivity, however this method (along with many others) often leaves residual catalyst impurities in the final product. These can be removed, typically with acids, however the discrepancies that exist between the SWCNT materials used in different studies can affect reproducibility and may have also hindered progress in this area.

Despite the fact that a number of species have been encapsulated within single-walled (SWCNTs) and double-walled nanotubes (DWCNTs), examples of electrochemical reactions successfully performed within these nanotubes are relatively rare in the literature. In contrast, applications of redox active nanoparticles confined within multiwalled carbon nanotubes for energy conversion and catalysis have been more widely explored.[8, 10] However, any further progress is significantly dependent on the understanding of fundamental questions essential for electrochemistry at the scale of 1-2 nm, within narrow CNTs, such as, but not limited to: host-guest charge transfer, mass transport effects, ion desolvation and through-wall charge compensation, which all still largely remain unresolved. This article reviews the status of confinement effects on redox active molecular species confined within single and double walled carbon nanotubes with internal diameters of 1-2 nm.

Fullerenes

Early studies into the specific electronic properties of redox active materials with discrete faradaic processes confined within CNTs were based on C_{60}@CNT. Being one of the first molecules to be encapsulated within SWCNTs[11] this hybrid material was widely explored in the late 1990s and 2000s. The rich redox chemistry of fullerenes enabled doping effects in nanotubes through chemical and heterogenous charge transfer methods to be studied, yet the discrete, reversible electrochemical reduction of the encapsulated C_{60} molecules was first explored in 2002. Kavan *et al.* reported the first studies into reducing C_{60} guest-molecules within SWCNTs.[12] Fullerene C_{60} is known to undergo chemical reduction to fulleride anions, for example when treated with potassium vapours, forming polymeric

chains of $[K^+]_{6n}(C_{60}^{6-})_n$ which had displayed similar conductivity to metallic materials;[13] the authors attempted to reproduce these results with an applied potential bias in C_{60}@SWCNT (Figure 2). Cyclic voltammograms (CVs) of the "peapod" (common early terminology for C_{60}@SWCNT materials) material in acetonitrile with a 0.2M $LiClO_4$ supporting electrolyte appeared completely analogous to that of empty SWCNTs, with none of the reversible redox processes of the encapsulated C_{60} observed. The authors attributed the lack of C_{60} faradaic processes to poor penetration of Li^+ ions to the C_{60} sites upon reduction, required to compensate the negative charge deposited onto the fullerenes (Figure 3a). Another alternative is for the charge-balancing cation to interact with the C_{60}^{n-} *via* a "through- wall" interaction, where the charge balancing may be fulfilled by the ion simply adsorbing onto the exterior SWCNT sidewall (Figure 3 b). This was considered by the authors to be insufficient to balance charge due to the negative charging of the SWCNT surface required to allow the approach of hydrated Li^+ ions. Nevertheless, the authors observed, *via* Vis-NIR absorption spectroscopy and Raman spectroscopy, electrochemical bleaching (removing the SWCNTs from resonance conditions) of the transitions between Van Hove singularities with applied potentials (both anodic and cathodic) through the population and depopulation of the SWCNT density of states (DoS). This bleaching effect additionally led to an increase in the intensity

of the C_{60} Raman bands upon anodic charging of the system, which could not be reported for the cathodic charging of the system. The authors later reported similar results in C_{70}@SWCNT, however the same increase in intensity of the fullerene Raman bands was not observed upon anodic charging of the C_{70}@SWCNT peapods.[14, 15]

A later study published by Sun *et al.* reported the first observation of faradaic processes from encapsulated molecules in C_{60}@SWCNT and C_{70}@SWCNT materials.[16] Overall the authors were able to probe three reversible processes in the peapod materials in acetonitrile with a 0.1M $[Bu_4N]ClO_4$ supporting electrolyte, which corresponded to C_{60}/C_{60}^{-}, C_{60}^{-}/C_{60}^{2-} and C_{60}^{2-}/C_{60}^{3-} respectively (Figure 3, c & d). Accessing the third process at the widest potential range appeared to destabilise the electrode, decreasing the current associated with redox processes of the guest-molecules in the subsequent scan, demonstrating the limited stability of the material upon repeated potential cycling in the range between –0.4 and –2.5 V *vs* Fc/Fc^{+}. When the potential window was restricted to between –0.4 and –1.6 V *vs* Fc/Fc^{+} two of the encapsulated fullerene redox process could be observed and appeared more stable over repeated cycling. Linear increases of the faradaic current were observed with increasing scan rate,

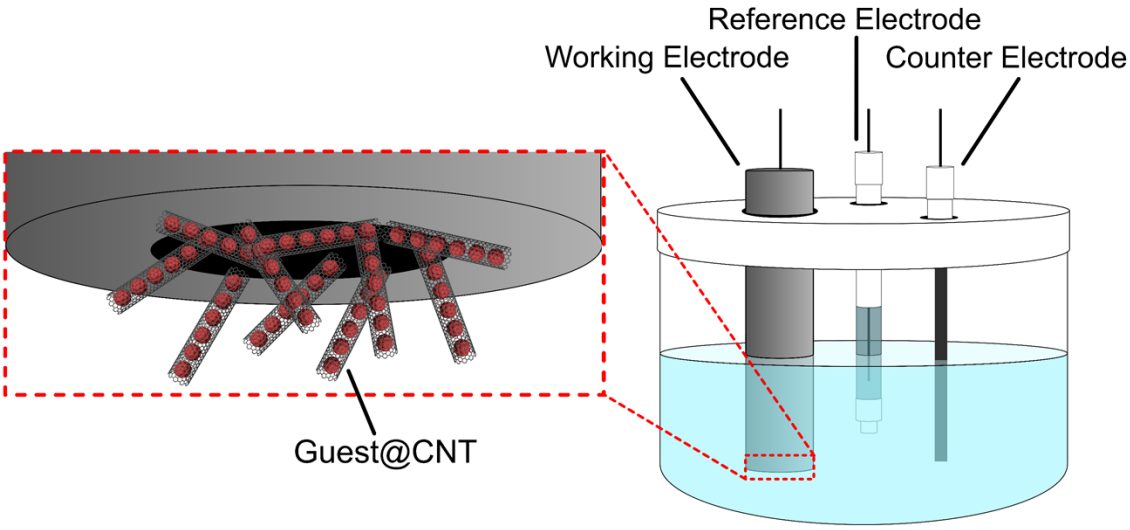

Figure 2. Schematic diagram of a typical three-electrode electrochemical cell setup for CV measurements of redox reactions inside nanotubes, showing a thin film of carbon nanotubes filled with guest-molecules on a working electrode surface, magnified for clarity; electrode and nanomaterials not to scale.

demonstrating the surface bound nature of the redox processes. The full width at half maximum (FWHM) of the redox waves were wider than what would be expected for a single electron surface bound process (90.6 mV at 25 ^{O}C), which the authors suggested was likely due to the favourable interactions between the guest-molecule and host-nanotube, which can shift redox processes and alter their idealised wave-shapes.[17] Cycling the material repeatedly over the –0.4 to –1.6 V *vs* Fc/Fc^{+} potential window eventually led to loss of all faradaic processes in the material, despite C_{60} still being encapsulated in the nanotube, as confirmed with transmission electron microscopy (TEM) imaging, suggesting that it could have been due to an increase in the resistivity of the material deposited on the electrode.

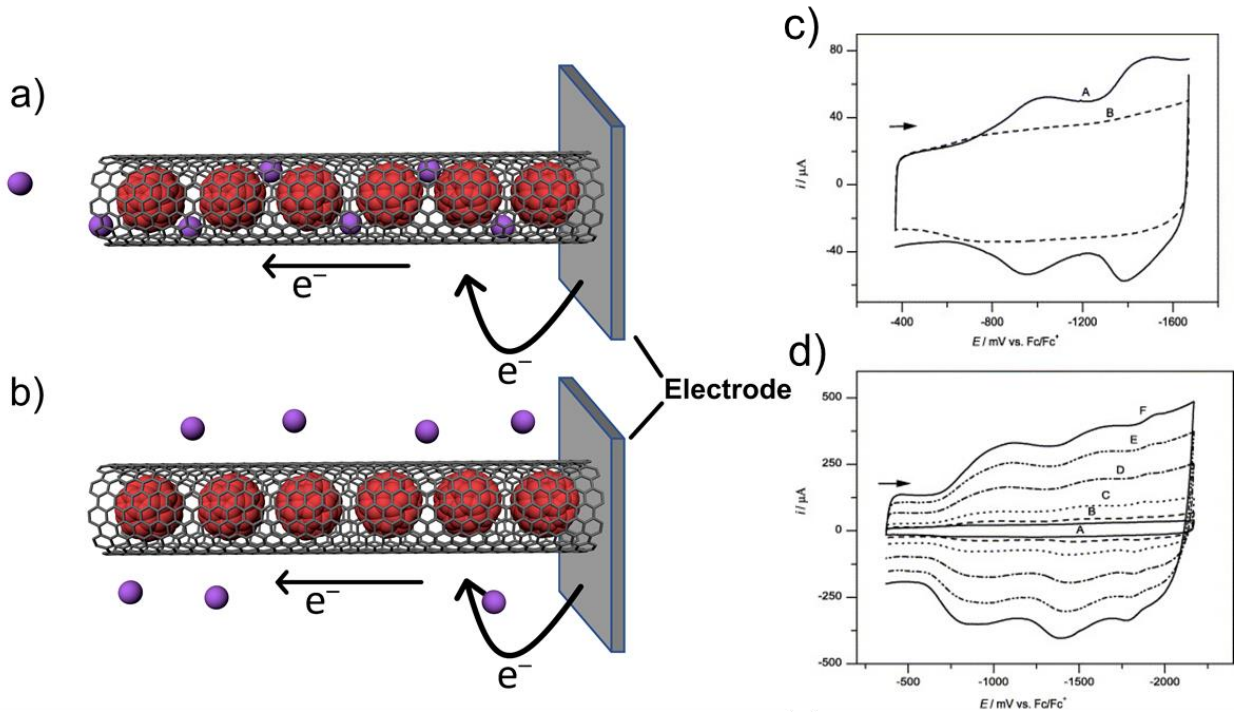

Figure 3. Schematics of (a) electrolyte cation insertion to balance charge on reduced fullerenes, and (b) through-wall charge compensation (purple circles are cations). (c) Cyclic voltammograms of C_{60}@SWCNT (plot A) and empty SWCNT (plot B) recorded in acetonitrile with a 0.1M $[Bu_4N]ClO_4$ supporting electrolyte at a scan rate of 0.1 V s^{-1}. (d) Cyclic voltammograms of C_{60}@SWCNT recorded under the same conditions at increasing scan rates (0.05 V s^{-1} to 0.5 V s^{-1}). Reproduced from reference 16, with permission from Elsevier, copyright 2005.

Additionally, the authors attempted to explain the lack of faradaic processes in the work published previously by Kavan *et al.* by altering the supporting electrolyte in the cell. The authors saw the loss of

faradaic processes when utilising $LiClO_4$, the same as Kavan *et al.*, suggesting that solvated Li^+ ions could not sufficiently penetrate to the reduced C_{60} species, as previously discussed, yet Bu_4N^+ cations could.[12] When altering the anion of a Bu_4N^+ electrolyte between ClO_4^- and PF_6^- faradaic processes from the encapsulated C_{60} molecules were seen in both cases, indicating that it was the role of the cation that was more significant for accessing the redox processes of guest-C_{60} and C_{70} molecules encapsulated within the host-nanotube. The authors suggested that upon reduction of C_{60}@SWCNT to C_{60}^-@SWCNT, Bu_4N^+ could readily enter the SWCNT to compensate the charge of the reduced fullerene molecules, forming $[Bu_4N^+][C_{60}^-]$@SWCNT. X-Ray photoelectron spectroscopy (XPS) of the C_{60}@SWCNT and C_{70}@SWCNT materials after repeated cycling showed the presence of XPS peaks for nitrogen atoms in two different environments, rather than the single environment observed if a peapod electrode was dipped into the electrolyte solution, suggesting that the Bu_4N^+ cations had become intercalated within nanotubes during cycling. Experiments conducted with aqueous electrolytes were devoid of fullerene faradaic processes, suggesting that the choice of electrolyte solvent also effected the redox processes of guest-molecules confined within host-nanotubes.

Perhaps a critical piece of the puzzle concerning early work on the observed faradaic activity in peapods is the pre-treatment of SWCNTs before fullerene encapsulation. Sun *et al.*[16] employed a vigorous acid treatment of the SWCNTs before fullerene encapsulation, with the purpose of introducing defects in the SWCNT sidewall allowing better access to fullerene molecules from the vapour phase during encapsulation, as had been demonstrated in other works.[18] Whilst these defects in the host-nanotube were necessary to increase access of the guest-molecules to the SWCNT interior, they could have had important implications for access of ions during CV measurements, as noted by the authors. Still, this could not explain the absence of faradaic processes when changing Bu_4N^+ to Li^+ in acetonitrile as their Stokes radii, which include the solvation shell, are 3.86 Å[19] and 2.98 Å[20] respectively, with the former approaching the van der Waals radius of C_{60}.[9]

In a later work Wu *et al.* demonstrated that C_{60} could be electrochemically addressed during CV measurements inside double-walled carbon nanotubes (C_{60}@DWCNT).[21] Altering the cation of the electrolyte between Li^+, Me_4N^+, Pe_4N^+ and Bu_4N^+ the authors demonstrated again that the redox behaviour of the encapsulated fullerenes was highly dependent on the choice of supporting electrolyte. Only when using a Bu_4N^+ and Pe_4N^+ supporting cation were redox processes observed from the encapsulated fullerenes. However, the results with Pe_4N^+ showed extremely large peak to peak separations for all redox processes, indicative of poor electron transfer in surface confined redox processes. Performing a similar XPS experiment to that described earlier, the authors showed that Me_4N^+ was not readily intercalated between the C_{60} molecules encapsulated within the DWCNTs, whereas Bu_4N^+ was, based on the multiple N environments observed after electrochemical cycling. This is perhaps counter intuitive, especially when considering the groups similar work on C_{60}@SWCNTs, as Bu_4N^+ is larger than Me_4N^+ (Stokes radius 2.52Å in acetonitrile) suggesting that the mass transport of Bu_4N^+ ion should be expected to be more inhibited. The internal diameter of the DWCNTs used in the study from analysis of the TEM images provided in the paper appear to be ~2.5 nm, which when partially blocked with C_{60}, as shown in the images, would likely restrict the mass transport of the larger quaternary ammonium cations to the site of the reduced fullerene (Figure 4, a & b). Steric restriction for quaternary ammonium cation transport in SWCNTs filled with C_{60} that allows a van der Waals gap of 0.3 nm[11] (i.e. no physical space between the guest- molecule and nanotube wall; Figure 4 a & b) should be expected to be more severe, preventing the transport of the Bu_4N^+ along the nanotube channel toward the reduced fullerenes, suggesting that through-wall charge compensation was significant.

Studies carried out by the Kawasaki group on the lithium-ion storage capacity[22] and sodium-ion storage[23] capacity of C_{60}@SWCNT report on the ability of alkali metal cations to penetrate the interior of the peapod structure, with both papers reporting higher reversible capacities for peapod materials *versus* that of empty SWCNTs for both Li^+ and Na^+ ion storage. The authors suggested that Li^+ ions were inserted during electrochemical charging, when utilising a $LiClO_4$ supporting electrolyte dissolved in an ethylene-carbonate (EC) and diethyl- carbonate mixture (DEC) (1:1). Whilst the Stokes radius of Li^+ is known to be significantly larger than Na^+ in many solvents[20] the authors were unable to establish a mechanism that led to the increase in sodium ion storage in the latter example *versus* empty SWCNTs, suggesting that there was no definitive evidence to support intercalation of lithium ions into the nanotube interior, upon the formation of encapsulated fullerides, during charging. In both cases the group discussed the possible

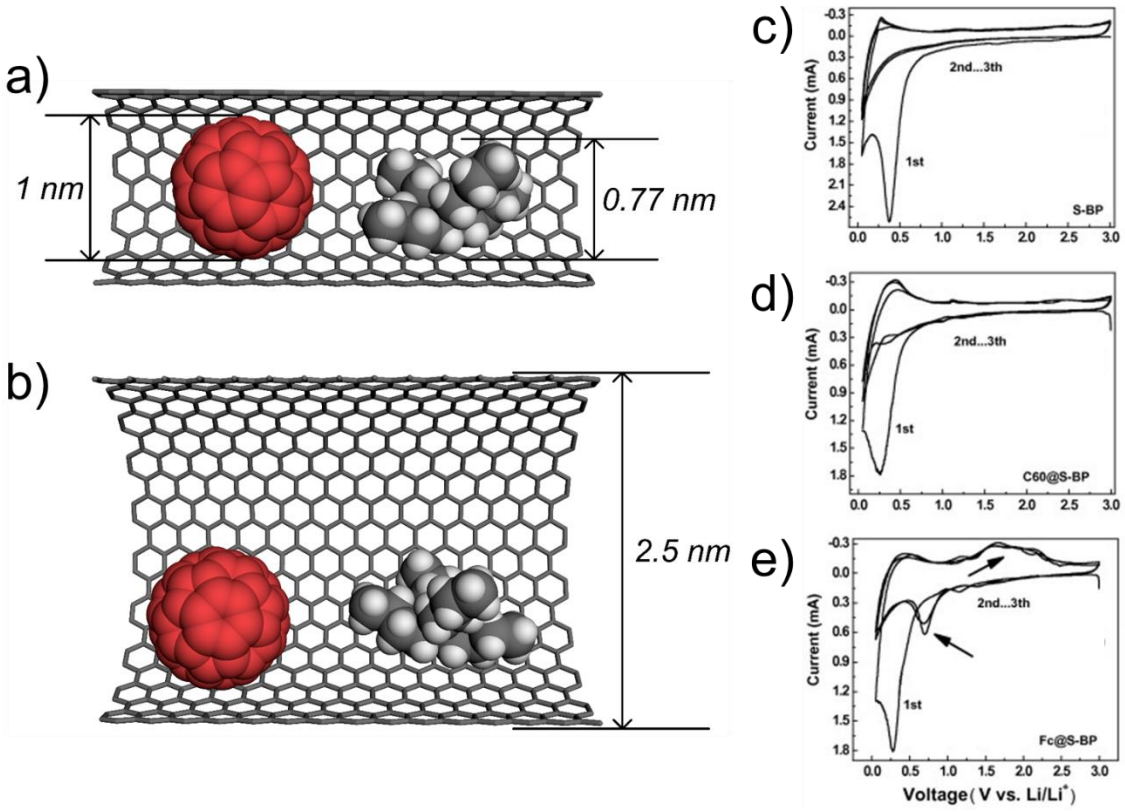

Figure 4. Schematic diagrams (a) of C_{60} and Bu_4N^+ within a narrow nanotube (van der Waals and Stokes diameter are shown respectively), (b) of C_{60} and Bu_4N^+ within a wider nanotube (such as a DWCNT) for comparison. CV measurements for SWCNT, C_{60}@SWCNT and $FeCp_2$@SWCNT (c-d respectively) acquired with a 1M $LiPF_6$ supporting electrolyte dissolved in DC:EC:EMC (1:1:1) at a scan rate of 0.4 mV s^{-1}. Reproduced from reference 24 with permission from Elsevier, copyright 2010.

presence of a surface electrolyte interface (SEI) layer close to the SWCNT ends where the ions could be desolvated, thus lowering the steric barrier of cation transport along the SWCNT. Notably the insertion of Li^+ ions was only observed at slow charging rates, suggesting that the process was kinetically inhibited. Likening the interior SWCNT sidewall to that of the basal plane of graphite the authors argued that an empty SWCNT interior presents an unfavourable surface for Li^+/Na^+ adsorption, whereas the peapod structure contained many suitable sites for cation adsorption, such as cavities between two neighbouring fullerenes leading to the observed increase in ion-storage capacity in the peapods. The study however did not report redox processes in the CV corresponding to C_{60} guest- molecules.

The lithium ion storage capacity of SWCNTs was similarly increased by the incorporation of C_{60} and ferrocene within SWCNTs ($FeCp_2$, Cp = cyclopentadiene) in a publication by Li *et al.* in 2010.[24] Largely in agreement with the earlier results from the Kawasaki group, CVs of the SWCNT, C_{60}@SWCNT and $FeCp_2$@SWCNT materials (Figure 4, c-e) in a $LiPF_6$ supporting electrolyte dissolved in a ethylene carbonate (EC), dimethyl carbonate (DC) and ethylmethyl carbonate (EMC) mixture showed a single reduction on the first CV cycle which was not reversible in the SWCNT or C_{60}@SWCNT materials, and was lost on subsequent scans. The return scan for $FeCp_2$@SWCNT showed a reversible oxidation which was relatively stable, and the initial reduction was also observed over multiple CV cycles instead of being lost after the first cycle. These redox processes were attributed to lithium diffusion into the SWCNT interior space, citing papers from Wang[25] and Shimoda[26] that showed similar reversible redox processes for SWCNTs used in Li cells. Li *et al.* suggested that these processes were only seen for $FeCp_2$@SWCNT due to desolvation of Li^+ at the nanotube entrance and therefore a lower barrier to Li^+ transport within the SWCNT compared to C_{60}@SWCNT. However, the possibility of redox processes of the encapsulated $FeCp_2$ molecule itself was not considered in the work.

Table 1. Redox reactions of fullerenes confined within carbon nanotubes.

Materials and Redox process	CNT diameter & synthesis method	Observation	Electrode	Range of potentials	Electrolyte	Ref.
C_{60}@SWCNT	~1.5 nm SWCNTs. Laser ablation with Ni/Co catalyst.	No redox process observed.	Thin film electrode of peapods on Pt sheets. Pt counter electrode (CE) and Ag-wire pseudo-reference electrode.	–1.5 to +1.5 V vs Ag/AgCl.	$LiClO_4$ 0.2M in CH_3CN.	12 (Kavan)
C_{60}@SWCNT	~1.5 nm SWCNTs. Laser ablation with Ni/Co catalyst.	No redox process observed.	Thin film electrode of peapods on Pt sheets. Pt CE and Ag- wire pseudo-reference electrode.	–1.65 to +1.15 V vs Ag/AgCl at 0.1 V/s.	$LiClO_4$ 0.2M in CH_3CN.	14, 15(kavan)
C_{60}@SWCNT + $e^- \rightarrow$ [C_{60}^-]@SWCNT [C_{60}^-]@SWCNT + $e^- \rightarrow$ [C_{60}^{2-}]@SWCNT [C_{60}^{2-}]@SWCNT + $e^- \rightarrow$ [C_{60}^{3-}]@SWCNT	~1.5 nm SWCNTs. Arc-discharge with Y/Ni catalyst.	Reversible redox processes at $E_{1/2}$= – 0.97 V, $E_{1/2}$= – 1.42 V and $E_{1/2}$= – 1.85 V vs Fc/Fc^+ for C_{60}/C_{60}^-, C_{60}^-/C_{60}^{2-} and C_{60}^{2-}/C_{60}^{3-} respectively. Rapid degradation of electrode over cycling. Bu_4N^+ proposed to enter into nanotubes.	Thin film electrode of peapods on glassy carbon. Ag/AgCl wire or KCl SCE reference electrode (RE), Pt wire CE.	– 0.4 to +1.7 V vs Fc/Fc^+ at various scan rates.	Bu_4NClO_4 0.1 M in CH_3CN.	16 (Sun)
C_{60}@DWCNT + $e^- \rightarrow$ [C_{60}^-]@DWCNT [C_{60}^-]@DWCNT + $e^- \rightarrow$ [C_{60}^{2-}]@DWCNT [C_{60}^{2-}]@DWCNT + $e^- \rightarrow$ [C_{60}^{3-}]@DWCNT	~2.5 nm internal diameter DWCNTs. Arc-discharge with FeS catalyst KCl promoter.	Reversible redox process with Bu_4NClO_4. No redox processes with $LiClO_4$ and Me_4NClO_4 equivalents.	Thin film electrode of peapods on glassy carbon. Ag/AgCl wire or KCl SCE RE, Pt wire CE.	– 2 to – 0.2 V vs Fc/Fc^+ at various scan rates.	Bu_4NClO_4 0.1 M in acetonitrile and toluene (1:4 v/v)	21 (Wu)
$FeCp_2$@SWCNT C_{60}@SWCNT	~1.4 nm SWCNTs. Arc-discharge with Y/Ni catalyst.	Plateaus in the charge–discharge curves were attributed to intercalation of Li^+ into the	Coin– type cell with peapod bucky paper cathode and lithium sheet anode, with a	0 to +3 V vs Li/Li^+.	1M lithium hexafluorophosphate ($LiPF_6$) in a mix of ethylene carbonate	24 (Li)

		SWCNT interior rather than specific redox processes of encapsulated material.	celgard 2300 membrane separator.		(EC):ethyl methyl carbonate (EMC):dimethyl carbonate (DMC)(1:1:1 v/v).	

Metallocenes

Ferrocene ($FeCp_2$) undergoes rapid heterogenous charge transfer in solution associated with the Fe^{2+}/Fe^{3+} redox couple. Its well-defined oxidation potential means that it is routinely used as an internal reference in cyclic voltammetry experiments and has also found use as a charge mediator in electrochemical systems. Combined with the fact that the size of $FeCp_2$ molecules is compatible with the interior of SWCNTs, several groups began to investigate the encapsulation and redox chemistry of $FeCp_2$ confined within carbon nanotubes in the mid- 2000s.

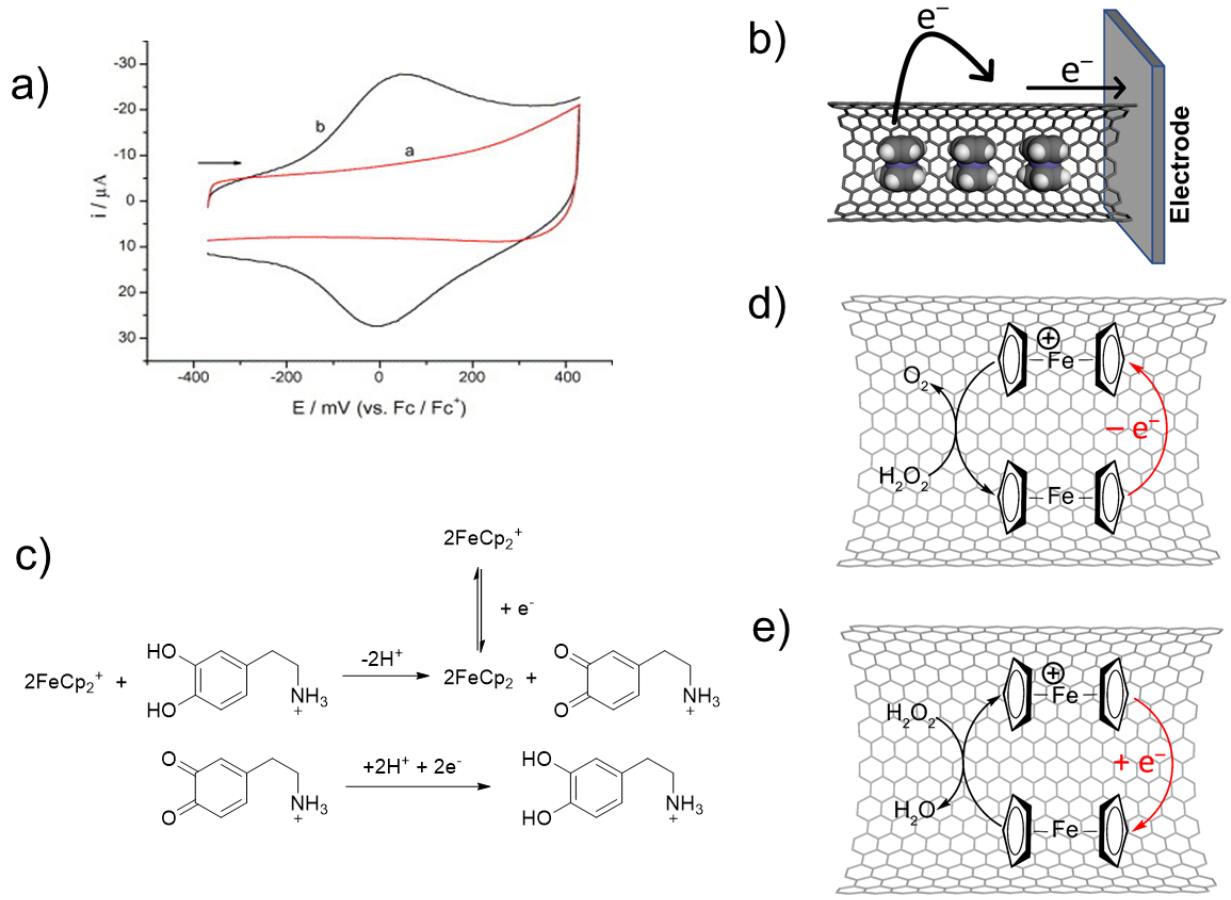

Figure 5. (a) Cyclic voltammograms of SWCNTs (a, red) and $FeCp_2$@SWCNT (b, black) in acetonitrile with a 0.1M $[Bu_4N]ClO_4$ supporting electrolyte at a scan rate of 0.05 V s^{-1}. Reproduced from reference 27 with permission from Elsevier, copyright 2005. (b) Schematic representation of electron (black arrows) flow during $FeCp_2$@SWCNT electrochemical oxidation. (c) reaction scheme depicting the electron mediated oxidation of dopamine via ferrocene encapsulated within DWCNTs. (d) reaction scheme depicting the oxidation of H_2O_2 by encapsulated ferrocene. Heterogenous charge transfer is shown in red. (e) reaction scheme depicting the reduction of H_2O_2 by encapsulated ferrocene. Heterogenous charge transfer is shown in red.

The first report of encapsulated ferrocene within SWCNTs ($FeCp_2$@SWCNT) and observations of confined electrochemistry were reported by Guan *et al.* in 2005.[27] The group achieved encapsulation *via* a vapour diffusion process, similar to that used to produce C_{60}@SWCNT. The single reversible oxidation process of ferrocene in solution was observed in $FeCp_2$@SWCNT, (Figure 5, a & b), proving that encapsulated ferrocene could be electrochemically addressed. The group utilised a $[Bu_4N]ClO_4$ electrolyte dissolved in acetonitrile and reported a linear increase of the peak currents *versus* scan rate similar to that of encapsulated C_{60}@SWCNT.

Infra-red (IR) spectroscopy measurements of the material showed a red shift of the C-H stretching mode of the cyclopentadienyl groups of the ferrocene molecule upon encapsulation, and a blue shift of the C-C bonds in the SWCNT, suggesting a partial charge transfer between the guest and host. This hypothesis was further evidenced by the wide FWHM values of the ferrocene redox process. The group utilised the encapsulated ferrocene as a source of carbon to form a second internal nanotube by heating the material to decompose the encapsulated ferrocene with the iron centres catalysing the reaction. Later studies by the group showed that the encapsulation of ferrocene within DWCNTs led to narrower FWHM values, which were attributed to less favourable interactions, namely π- π stacking and van der Waals forces, between the ferrocene molecules and the much wider DWCNTs.[28]

The same group later utilised $FeCp_2$@SWCNT in a second piece of work[29] by applying this material for H_2O_2 sensing, using the encapsulated ferrocene molecules as charge mediators in the reduction and oxidation of hydrogen peroxide in solution. The effect of the electrolyte on the CV profile of $FeCp_2$@SWCNT, was studied with $LiClO_4$, LiCl, KCl, KH_2PO_4, Na_2HPO_4 and $[Bu_4N]Br$ as 0.1M aqueous solutions. In contrast to C_{60}@SWCNT, the group found that the best current response was achieved for $LiClO_4$, which is consistent with previous work by Claye *et al.* that demonstrated the reversible insertion of lithium ions into empty SWCNTs.[30] However, it is important to remember that unlike fullerenes, ferrocene undergoes a reversible

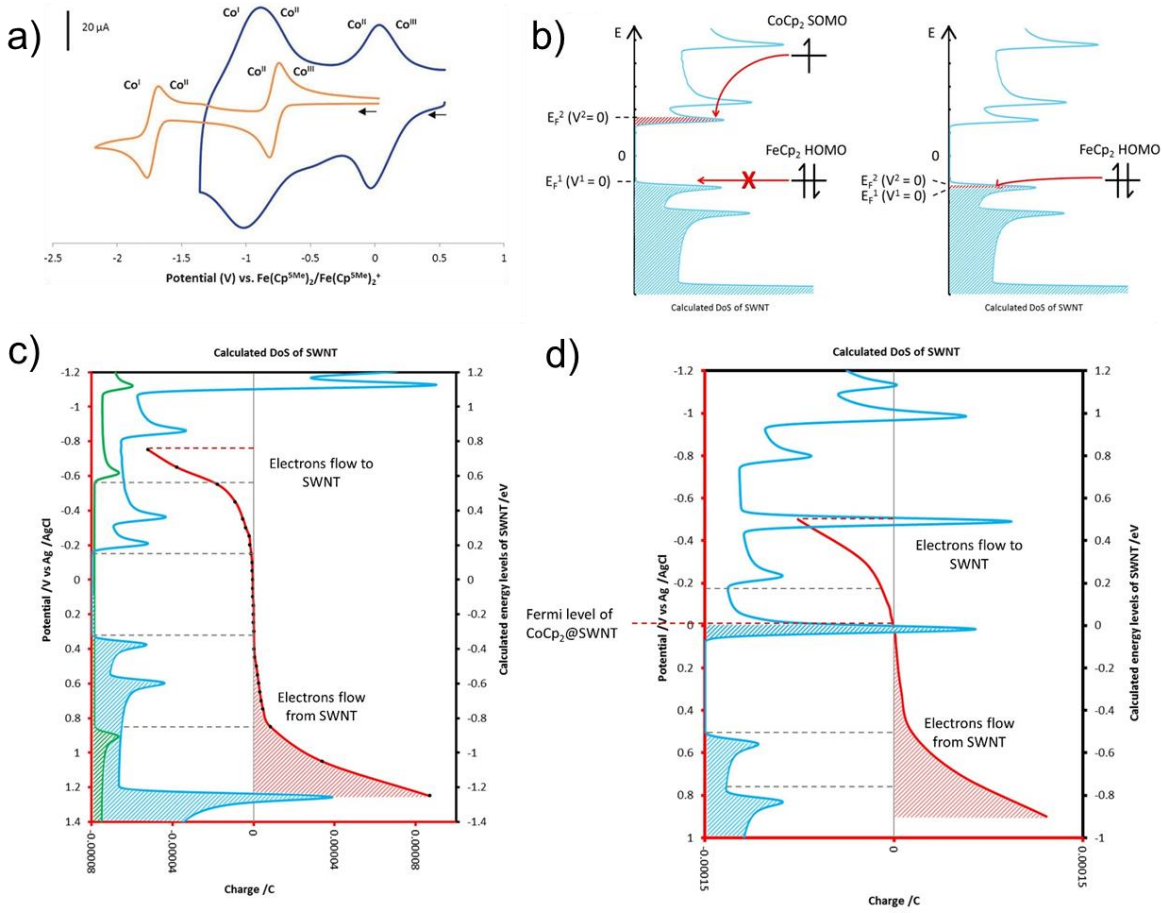

Figure 6. (a) CV measurements for $CoCp_2$ (orange) and $CoCp_2$@SWCNT (blue) recorded in acetonitrile with a 0.1M $[Bu_4N]PF_6$ supporting electrolyte at a scan rate of 0.1 V s^{-1}. (b) The direction of charge transfer between bands of SWCNT and molecular orbitals of encapsulated metallocenes. Chronoamperometry measurements of SWCNTs (c) and $CoCp_2$@SWCNT (d). Figure adapted from ref 33, with permission from Wiley, copyright 2016.

oxidation, possibly leading to the anion of the electrolyte having a more considerable effect on any observed redox processes. An increase in cycling stability was demonstrated by cycling $FeCp_2$@SWCNT over 4000 potential cycles in a range of -0.2 to +0.8 V vs SCE, with 80% of the faradaic current being lost at the end of the cycling experiment. Additionally, the authors noted the influence of the electrolyte anion on the observed redox chemistry, demonstrated by poorer potential cycling stability and lower current response when using LiCl, which the authors attributed to the lower stability of the ferrocenium ion ($[FeCp_2]^+$) in solutions of chloride salts. The addition of H_2O_2 to the electrolyte solution during cyclic voltammetry experiments led to an increase in both the anodic and cathodic peak currents for $FeCp_2$@SWCNT, which increased with increasing H_2O_2 concentration. The authors suggested that this was

due to the ferrocene mediated reduction and oxidation of H_2O_2 within the SWCNT, (Figure 5, d & e) indicating that the peroxide could readily access the encapsulated ferrocene redox centres. The group noted a shift in the Raman G-band of the host-nanotubes, indicative of charge transfer from the guest to host. The larger than expected FWHM values, which was attributed to favourable interactions between the SWCNT and encapsulated ferrocene molecules, further supported the presence of effective host-guest interactions in $FeCp_2$@SWCNT.

$FeCp_2$@DWCNT was later applied to dopamine sensing.[31] The work reported by Cheng *et al.* demonstrated that $LiClO_4$ was still an optimal electrolyte due to the ability of Li^+ to intercalate with the DWCNTs, and the weak coordination of the ClO_4^- anion to the positively charged ferrocenium ions. There were large peak-to-peak separations even at slow scan rates of 5 mV s^{-1}, which the authors attributed to the resistance of the DWCNTs. Peak current increased linearly with increasing scan rate as expected for solid state redox processes, but larger than expected FWHM values were reported too, again attributed to favourable $\pi-\pi$ interactions between the Cp group and interior DWCNT sidewall. Upon the addition of dopamine to the electrolyte solution the authors observed large anodic currents (oxidation of $FeCp_2$ to $FeCp_2^+$) and reduced cathodic currents ($FeCp_2^+$ to $FeCp_2$) in the $FeCp_2$@DWCNT redox cycle, with effects becoming more pronounced with increasing dopamine concentration. The native redox processes of dopamine were seemingly suppressed by the $FeCp_2$@DWCNT electrode, which the authors attributed to the localised pH within the DWCNT decreasing as the reaction proceeded (Figure 5c). This demonstrated that $FeCp_2^+$ formed inside nanotubes via the heterogenous charge transfer during the CV measurement could effectively oxidise dopamine molecules, hence reducing the return cathodic current. The group later applied $FeCp_2$@SWCNT to the same reaction, reporting similar results.[32]

Work carried out in our group, reported in 2016 by McSweeney *et al.* employed metallocenes encapsulated within SWCNTs to probe the host-guest charge transfer interactions between metallocenes

and SWCNTs *via* cyclic voltammetry and chronoamperometric methods.[33] Encapsulation of cobaltocene and different methylated ferrocenes ($Fe(Cp^{xMe})_2$, x = 0, 1, 4 and 5) in carbon nanotubes enabled CV measurements of these molecules confined within SWCNTs to be carried out with a 0.1M $[Bu_4N]BF_4$ in acetonitrile. Both the single electron reduction and oxidation processes of the cobaltocene (Co^{2+}/Co^{+} and Co^{2+}/Co^{3+} respectively) could be accessed upon encapsulation as well as the single oxidation of the ferrocene and its derivatives (Fe^{2+}/Fe^{3+}). Large positive shifts (~770 mV) in potentials of the redox processes in $CoCp_2$@SWCNT were observed as compared to free molecules in solution, (Figure 6a) indicative of significant electron transfer from the guest to host, leading to an overall n-doping effect of the SWCNT hosts, and formation of cobaltocenium cations as was demonstrated earlier by spectroscopic methods for $CoCp_2$@SWCNT.[34] For ferrocenes encapsulated within nanotubes, the shifts in the potential of the oxidation processes were far more subtle, ranging between 0 mV for $FeCp_2$@SWCNT and +200 mV for $Fe(Cp^{5Me})_2$@SWCNT correlating with an increasing number of methyl groups on the cyclopentadiene ligands. The shifts in the redox processes of both the cobaltocene and ferrocene were studied with linear sweep voltammetry (LSV) and chronoamperometry of the metallocene@SWCNT materials, using empty SWCNTs to provide an experimental profile of the density of states (DoS) of the host nanotubes.[35] Utilising LSV data, the DoS of the SWCNTs could be estimated, allowing the energies of the Fermi level (akin to the highest occupied molecular orbital, HOMO) and bottom of the conduction band (akin to the lowest unoccupied molecular orbital, LUMO) to be determined (Figure 5b). Cyclic voltammetry of the metallocenes acquired in identical conditions was carried out to estimate the energy levels of the singly occupied molecular orbital (SOMO) of $CoCp_2$ and the HOMO of $Fe(Cp^{xMe})_2$ and predict charge transfer.[36] From these experiments the comparison of energy levels could be carried out for the host and the guest, predicting the direction of charge transfer from cobaltocene to the conduction band of SWCNT, and from ferrocene to depleted levels of the valence band of SWCNT (due to oxygen containing surface groups on the SWCNT). Through modulation of the ferrocene structure, the direction and magnitude of this charge

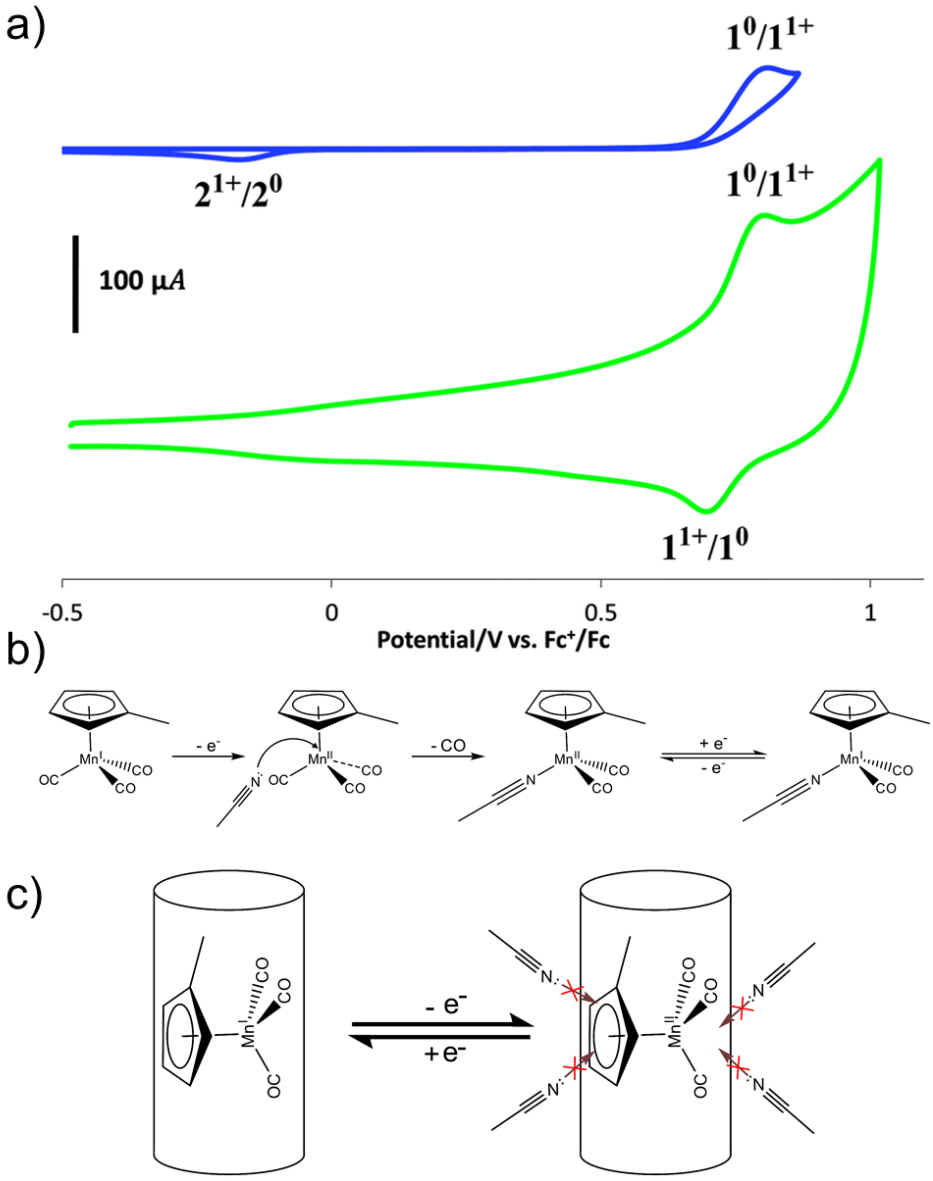

Figure 7. (a) Cyclic voltammograms of $Cp^{Me}Mn(CO)_3$ in solution (blue) and encapsulated within SWCNTs (green) recorded in acetonitrile with a 0.1 M $[Bu_4N]BF_4$ supporting electrolyte. Figure reproduced from reference 38, with permission from the Royal Society of Chemistry, copyright 2014. (b) The normal reaction pathway of $Cp^{Me}Mn(CO)_3$ in solution (a process corresponding to the blue CV trace above), and (c) a proposed reaction pathway for molecules confined within SWCNT (a process corresponding to the green CV trace above).

transfer could be specifically tuned. This was demonstrated with a series of methylated ferrocenes, $[Fe(Cp^{xMe})_2]$@SWCNT (x = 0, 1, 4, 5). Increasing the number of methyl groups increased the energy of the ferrocene HOMO, resulting in the observed shift in the Fe^{2+} to Fe^{3+} oxidation from 0.04 V for $FeCp_2$ to 0.20 V for $Fe(Cp^{5Me})_2$ *vs* Fc/Fc^+ (due to the inductive effect of methyl groups) in good agreement with the observed voltammetry discussed above. Furthermore, chronoamperometry measurements of the

metallocene@SWCNT materials (Figure 6, c &d) quantified the amount of charge transfer, which was indicated by changes in the charge passed upon encapsulation of the different metallocene species. This study was the first to utilise shifts in redox processes of encapsulated molecules and amperometric methods to accurately determine charge transfer direction and magnitude between the molecules and nanotubes, which was in good agreement with photoluminescence studies of metallocenes@SWCNT.[37] It is important to note that the focus of this investigation reported by McSweeney et al.[33] was on the electronic and steric relationship between the guest-molecule and host-nanotube, and the effect of the electrolyte or solvent was not explored, as in the examples in the previous section.

McSweeney *et al.* extended the electrochemistry of organometallic guest-molecules in nanotubes to a "piano- stool" manganese compound, $Cp^{Me}Mn(CO)_3$, where the host-nanotube was able to stabilise the complex undergoing an electrochemical oxidation, by altering the reactive pathway due to nanoscale confinement.[38] The complex $Cp^{Me}Mn(CO)_3$ typically undergoes a heterogenous one-electron oxidation (Mn^{+}/Mn^{2+}), at approximately 0.8 V *vs.* Fc/Fc^{+}, when utilising a 0.1M $[Bu_4N][BF_4]$ acetonitrile electrolyte. This yields the electron deficient $[Cp^{Me}Mn(CO)_3]^{+}$ species which can then react with acetonitrile, taking place via a nucleophilic substitution at the Mn^{2+} centre, leading to the loss of a CO ligand, and forming $[Cp^{Me}Mn(CO)_2(NCCH_3)]^{+}$. This is then reduced to $Cp^{Me}Mn(CO)_2(NCCH_3)$ at a more negative potential (–0.18 V) than the initial oxidation of the $Cp^{Me}Mn(CO)_3$ complex. By encapsulating the reactive $Cp^{Me}Mn(CO)_3$ complex within SWCNTs, the authors demonstrated that the encapsulated $Cp^{Me}Mn(CO)_3$ was reduced at a similar potential to the initial oxidation. (Figure 7, a) The authors attributed this change in the reduction potential to the steric hinderance on the nucleophilic attack of acetonitrile on $[Cp^{Me}Mn(CO)_3]^{+}$@SWCNT due to the confinement, essentially protecting the oxidised form of the complex during CV and allowing rapid reduction of the species at a similar potential to the initial oxidation (Figure 7, b & c). Therefore, there is a need to reconsider the simplistic view of the redox activity of molecules encapsulated within SWCNTs, where diffusion of solvent and electrolyte to/from the SWCNT is assumed to occur readily

towards the redox active centres, just like in a simple liquid phase CV measurement. For example, the apparent inconsistency of observed redox activity of fullerenes@SWCNT with the size of the electrolyte cation (e.g. higher redox activity in the presence of electrolyte with larger cations) would need to be considered in conjunction with the knowledge of redox processes of metallocenes@SWCNT.

Table 2. Redox reactions of metallocenes confined within carbon nanotubes.

Materials and Redox process	**CNT diameter & synthesis method**	**Observation**	**Electrode**	**Range of potentials**	**Electrolyte**	**Ref.**
$Fe^{II}Cp_2$@SWCNT → $[Fe^{III}Cp_2]^+$@SWCNT + e^-	~1.4 nm SWCNTs. Arc-discharge with Y/Ni catalyst.	Reversible redox process at $E_{1/2}$ = 20 mV vs Fc/Fc^+.	Thin film electrode of $Fe^{II}Cp_2$@SWCNT on glassy carbon., Ag/AgCl RE and Pt wire CE.	– 0.4 to +0.4 V vs Fc/Fc^+	$[Bu_4N]ClO_4$ 0.1 M in CH_3CN	27 (Guan)
$Fe^{II}Cp_2$@DWCNT → $[Fe^{III}Cp_2]^+$@DWCNT + e^-	~2.5 nm internal diameter DWCNTs. Arc-discharge with FeS catalyst KCl promoter.	Reversible redox process at $E_{1/2}$ = 384 mV vs Ag/AgCl. Much smaller ΔE_p than the SWCNT analogue. Peak currents are more stable on cycling than the $FeCp_2$@SWCNT sample.	Thin film electrode of $Fe^{II}Cp_2$@SWCNT on glassy carbon, Ag/AgCl RE and Pt wire CE.	– 0.1 to +0.9 V vs Ag/AgCl	$[Bu_4N]ClO_4$ 0.1 M in CH_3CN	28 (Qui)
$Fe^{II}Cp_2$@SWCNT → $[Fe^{III}Cp_2]^+$@SWCNT + e^-	~1.5 nm SWCNTs. Arc-discharge with Y/Ni catalyst.	Reversible redox process at $E_{1/2}$ = 283 mV. A range of electrolytes were screened with $LiClO_4$ giving the best response, with both the anion and cation affecting electrochemical stability. Li^+ is said to insert into the SWCNTs up to a stoichiometry of $Li_{1.23}C_6$.	Thin film electrode of $Fe^{II}Cp_2$@SWCNT on glassy carbon, SCE RE and Pt wire CE.	0 to +0.7 V vs SCE	$LiClO_4$ in H_2O	29 (Sun)
$Fe^{II}Cp_2$@SWCNT → $[Fe^{III}Cp_2]^+$@SWCNT + e^-	~1.4 nm SWCNTs. Arc-discharge with Y/Ni catalyst.	Reversible redox process at 0.52 V vs Fc/Fc^+. Quantification of electron transfer between the nanotube and	Thin film electrode of $Fe^{II}Cp_2$@SWCNT on glassy carbon, Ag/AgCl	0 to +1 V vs $Fc/Fc^=$	$[Bu_4N]BF_4$ 0.1M in acetonitrile	33 (McSweeney)

		guest-molecules.	RE and Pt wire CE.			
$[Co^{III}Cp_2]^+$@SWCNT + e^- → $Co^{II}Cp_2$@SWCNT $Co^{II}Cp_2$@SWCNT + e^- → $[Co^{I}Cp_2]^-$ @SWCNT	~1.4 nm SWCNTs. Arc-discharge with Y/Ni catalyst.	Reversible redox processes at $E_{1/2}$= – 0.96 V and 0.00 V vs Fc/Fc^+. Quantification of electron transfer between the nanotube and guest-molecules.	Thin film electrode of $Fe^{II}Cp_2$@SWCNT on glassy carbon, Ag/AgCl RE and Pt wire CE.	– 1.4 to +0.5 V vs Fc/Fc^+	$[Bu_4N]BF_4$ 0.1M in acetonitrile	33 (McSweeney)
$Cp^{Me}Mn^{I}(CO)_3$@SWCNT → $[Cp^{Me}Mn^{II}(CO)_3]^+$@SWCNT + e^-	~1.4 nm SWCNTs. Arc-discharge with Y/Ni catalyst.	Reversible redox process at 0.78 V vs Fc/Fc^+ at – 40 °C. Nanotube protects the guest- molecule from solvolysis during CV measurements.	Thin film electrode of $Fe^{II}Cp_2$@SWCNT on glassy carbon, Ag/AgCl RE and Pt wire CE	– 1 to +1 V vs Fc/Fc^+	$[Bu_4N]BF_4$ 0.1M in acetonitrile at – 40 °C	38 (McSweeney)

Organic Molecules

Most of the work on the encapsulation of medium-sized organic molecules for lithium-ion storage has been carried out by the Kawasaki group. In 2009 Kawasaki *et al.* reported on the encapsulation and lithium charge storage capacity of three organic molecules, 9,10-dichloroanthracene, β-carotene, and coronene, encapsulated within SWCNTs (Figure 8).[39] The authors reported that the encapsulation of all three organic molecules increased the overall capacitance *versus* empty SWCNTs, attributing this to the increased number of sites for Li^+ intercalation, similar to their work on C_{60}@SWCNT mentioned above. The capacities of each of the filled SWCNT materials were compared at varying current densities, and the capacity retention of SWCNTs with encapsulated organic molecules all appeared superior to empty SWCNTs when charged at higher current densities, indicating that the lithium transport was unhindered by the encapsulated organic molecules. The authors explained this counterintuitive observation by suggesting that filling of the carbon nanotube with an organic molecule could lead to the desolvation of Li^+ ions at the nanotube ends during charging and Li^+ insertion. The encapsulation of coronene, which has the largest

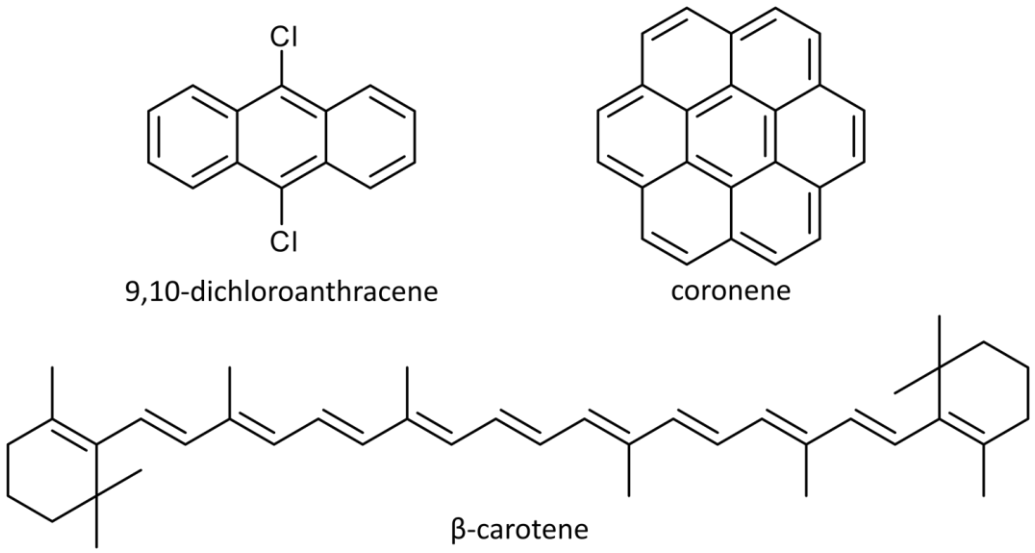

Figure 8. Structures of the compounds encapsulated within SWCNTs for lithium-ion storage in reference 39.

cross-sectional area of the organic molecules used in this study, led to the biggest increase in reversible capacity. This was attributed to the size of the molecule, leading to higher energy barriers to the transport of hydrated lithium ions and therefore more favourable desolvation of Li^+ at the coronene capped SWCNT ends and hence easier transport to the redox active sites within the nanotube (guest-molecules). The reversible capacity of the materials appeared to reduce little over 5 charge-discharge cycles.

Encapsulated quinones have also been explored as a charge storage material. A first report, published in 2016 by Ishii *et al.,* demonstrated the ability of 9,10-anthraquinone (AQ) and 9,10-phenanthrenequinone (PhQ) encapsulated within SWCNTs to store lithium ions (Figure 9, a).[40] Charge-discharge curves of the quinones loaded on to activated carbon, the SWCNT external surface and encapsulated within SWCNTs showed distinct plateaus for quinone reduction and oxidation when using a 1M $LiClO_4$ in ethylene carbonate and diethyl carbonate (1:1 v/v) supporting electrolyte (Figure 9, b-g). For the quinones encapsulated within SWCNTs the reversible capacities (based on the mass of active material) approached the theoretical maximum, suggesting that the majority of the encapsulated molecules were partaking in electrochemical processes. Additionally, the plateaus appeared to be more elongated when the redox active molecules were encapsulated within the SWCNTs *versus* loaded onto their external surfaces,

further strengthening this argument. The difference in the redox potential of the encapsulated *versus* surface bound quinone was negligible for PhQ but was around 50 mV for AQ, which can be explained by the interactions between AQ/PhQ and the SWCNT, as IR spectra revealed a blue shift of the carbonyl stretch for AQ@SWCNT, but not for PhQ@SWCNT. Despite this, both quinone@SWCNT materials

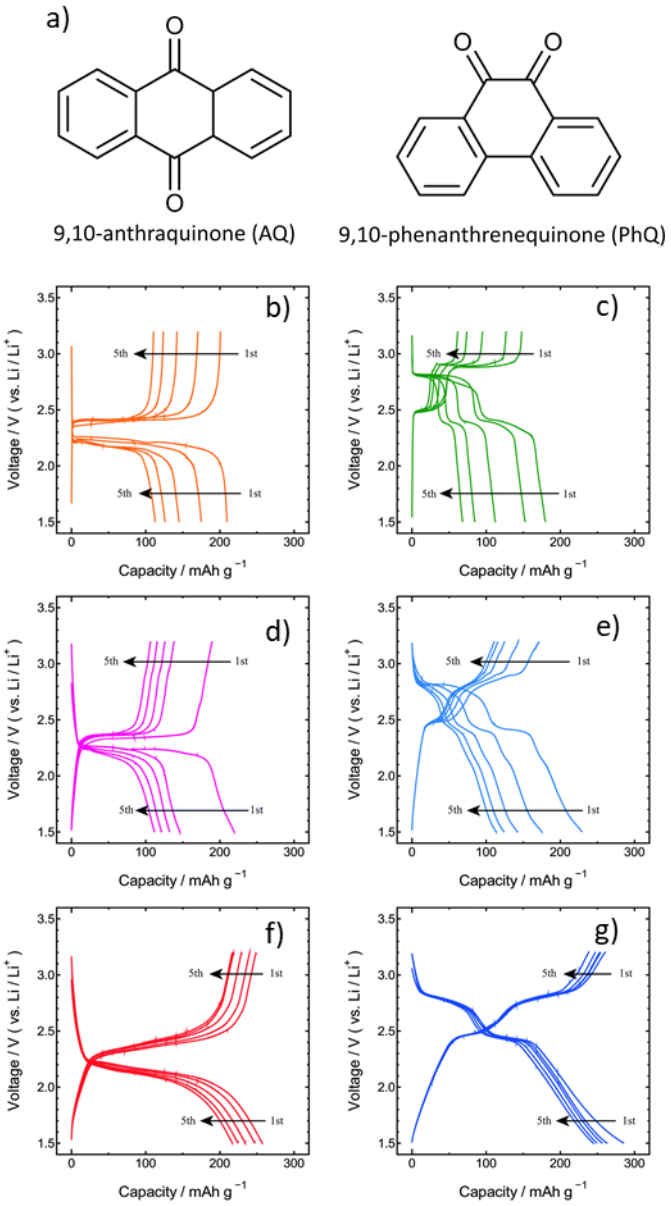

Figure 9. (a) Structures of AQ and PhQ. Charge-discharge curves of AQ/activated carbon, PhQ/activated carbon (b) and (c) respectively; AQ/SWCNT, PhQ/SWCNT (d) and (e) respectively, and AQ@SWCNT and PhQ@SWCNT (f) and (g) respectively. All measurements were performed with specific currents of 100 mA g^{-1} and capacities based on the weight of the active material only. Figure reproduced from reference 40 with permission from the Royal Society of Chemistry, copyright 2016.

benefited from improved capacity retention over 50 cycles upon encapsulation when compared to externally adsorbed quinone molecules, highlighting the benefits of encapsulation for these energy storage systems.

A study by Li *et al.* further investigated the application of the PhQ@SWCNT material for lithium and sodium ion storage (Figure 10, a).[41] In this study the authors encapsulated the quinone molecules in two different samples of SWCNT, with average diameters of 1.5 and 2.5 nm respectively. Encapsulation of PhQ within the smaller diameter nanotube gave a capacity that was close to the theoretical maximum for the molecule, yet encapsulation within the larger diameter SWCNTs led to a lower capacity of the material measured at around 50% of the theoretical value (Figure 10, b & c). The observation was attributed to the less favourable interactions between the wider SWCNT and the quinone molecule, indicating that electronic communication between the two was less efficient than in the narrower nanotubes. When comparing the sodium and lithium storage capacities of PhQ@SWCNT (Figure 10, d & e) the authors noted a small decrease in the overall capacity when utilising Na^+, with plateaus at similar potentials, although it appeared that the gradient of the plateaus had increased. When carrying out charge-discharge measurements at 0 ^oC there were further increases to the plateau gradients for both Li^+ and Na^+ storage, indicating less reversible ion intercalation, and there were small decreases in the overall capacity of the materials. More recently work published by Tsuzuki *et al.* applied density functional theory (DFT) calculations to investigate the mass transport of Li^+ ions in quinone@SWCNT materials.[42] The authors found that Li^+ could diffuse along the SWCNT interior sidewalls, as well as "hop" between the encapsulated quinone molecule storage sites, which was accompanied by considerable changes in the cross-sectional geometry of the SWCNT in their model. Li *et al*. later utilised iodine encapsulated in nanotubes alongside their previously reported quinone@SWCNT materials in a secondary battery, where the I@SWCNT (in the form of encapsulated linear chains of iodine) formed the cathode and PhQ@SWCNT formed the anode.[43] CVs of PhQ@SWCNT with a 1M LiI aqueous electrolyte showed only one reversible

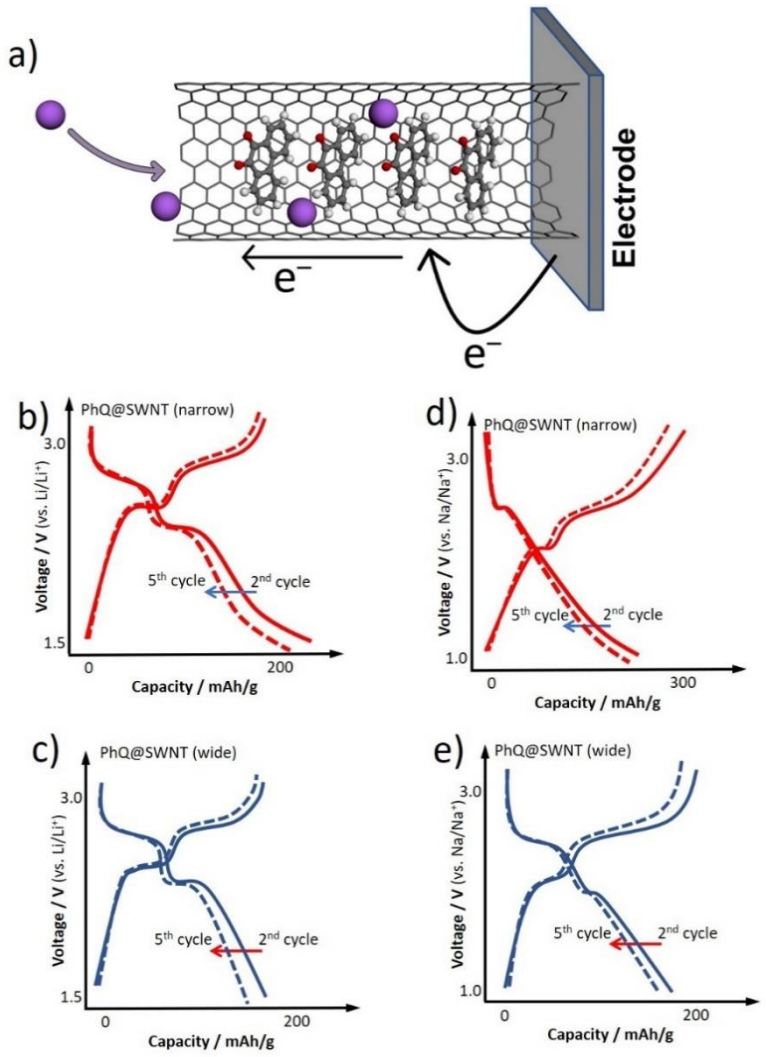

Figure 10. (a) Schematic diagram showing the flow of electrons and lithium ions during charging of PhQ@SWCNT. Charge-discharge curves for PhQ@SWCNT in narrow SWCNTs (b) and wider SWCNTs (c). Sodium storage charge-discharge curves for PhQ@SWCNT in narrow SWCNTs (d) and wider SWCNTs (e). Measurements were acquired with specific currents of 100 mA g^{-1}, capacity based on the mass of active material.

redox process, and the galvanostatic charge-discharge curves showed only one plateau, which was in contrast to previous work investigating PhQ@SWCNT in 1M $LiClO_4$ in EC/DEC, which showed two distinct plateaus. The authors explained the loss of the second redox process, and the decrease of capacity to approximately 50% of the theoretical maximum, by suggesting that only one C=O bond was lithiated. This change in redox behaviour and decrease in capacity when comparing the material in aqueous and organic electrolytes (used in their previous studies) was attributed to the polar water solvent molecules less

readily entering and diffusing along the hydrophobic environment inside the nanotube, thus reducing the amount of lithiation that could occur. When utilising NaI, there were no observed redox processes in the CV or charge-discharge curves and the overall capacity was lower, suggesting that the larger size of the Na^+ ion hindered its mass transport, however it must be noted that the hydrated radius of a Na^+ ion is smaller than a hydrated Li^+ ion.[44]

Table 3. Redox reactions of metallocenes confined within carbon nanotubes.

Materials and Redox process	**CNT diameter & synthesis method**	**Observation**	**Electrode**	**Range of potentials**	**Electrolyte**	**Ref.**
9,10–dichloroanthracene@SWCNT β– carotene@SWCNT coronene@SWCNT	~1.3 nm SWCNTs. Laser ablation.	Plateaus in the charge–discharge curves were attributed to intercalation of Li^+ into the SWCNT interior rather than specific redox processes of encapsulated molecules.	SWCNT wrapped in Ni mesh WE, Li metal plate as the pseudo reference and CE.	0 to +3 V vs Li/Li^+	1M $LiClO_4$ in EC	39 (Kawasaki)
PhQ@SWCNT + e^- → [PhQ^-]@SWCNT [PhQ^-]@SWCNT + e^- → [PhQ^{2-}]@SWCNT	~1.5 nm SWCNTs. Arc-discharge.	All encapsulated molecules electrochemically accessible. Increased stability upon encapsulation.	Two-electrode cell with a PhQ@SWCNT bucky paper on Cu- foil WE, Lithium foil CE, with a porous polypropylene film separator.	+1.5 to +3.2 V vs Li/Li^+	1M $LiClO_4$ in a mixture of diethyl carbonate (DC) and EC (1:1 v/v)	40 (Ishii)
AQ@SWCNT + e^- → [AQ^-]@SWCNT [AQ^-]@SWCNT + e^- → [AQ^{2-}]@SWCNT	~1.5 nm SWCNTs. Arc-discharge.	All encapsulated molecules electrochemically accessible. Increased stability upon encapsulation.	Two- electrode type cell with AQ@SWCNT bucky paper on Cu- foil WE, Lithium foil CE, with a porous polypropylene film separator.	+1.5 to +3.2 V vs Li/Li^+	1M $LiClO_4$ in a mixture of DC:EC (1:1 v/v)	40 (Ishii)
PhQ@SWCNT + e^- → [PhQ^-]@SWCNT [PhQ^-]@SWCNT + e^- → [PhQ^{2-}]@SWCNT	~1.5 nm SWCNTs. Arc-discharge with Y/Ni catalyst. ~2.5 nm SWCNTs. Gas phase CVD	Two kinds of SWCNT with different diameters utilised. Smaller nanotubes (d= 1.5 nm) gave higher capacities than larger nanotubes (d= 2.5 nm).	Two-electrode cell, with PhQ@SWCNT or AQ@SWCNT bucky paper on Cu- foil WE and Lithium/Sodium foil CE.	+1.5 to +3.2 V vs Li/Li^+	1M $LiClO_4$ in a mixture of DC:EC (1:1 v/v) or 1M $NaClO_4$ in propylene carbonate	41 (Li)

	method (eDIPS).					
PhQ@SWCNT + e^- → [PhQ^-]@SWCNT	~2.5 nm SWCNTs. Gas phase CVD method (eDIPS).	Only one plateau seen in the charge/discharge curves, assigned to only one Li^+/Na^+ ion coupled reduction process, as opposed to two in organic electrolytes (see table entry above).	Three-electrode cell, PhQ@SWCNT anode, empty SWCNT cathode and Ag/AgCl RE.	– 0.4 to +0.2 V vs Ag/AgCl	Aqueous 1M LiI or NaI	43 (Li)

Halogens

An early study on the electrochemical behaviour of halogens/halides encapsulated within nanotubes by Song *et al.* reported that I^- anions could be encapsulated within SWCNTs electrochemically, as observed by Raman spectroscopy and the increasing dispersibility of the SWCNTs in aqueous solvents.[45] The group further used I@SWCNT to study charge transfer between the SWCNT-host and iodide-guest.[46] Furthermore, Taniguchi *et al*. reported the increased capacitance of I@SWCNTs[47] and Br@SWCNT[48] compared to empty SWCNTs.

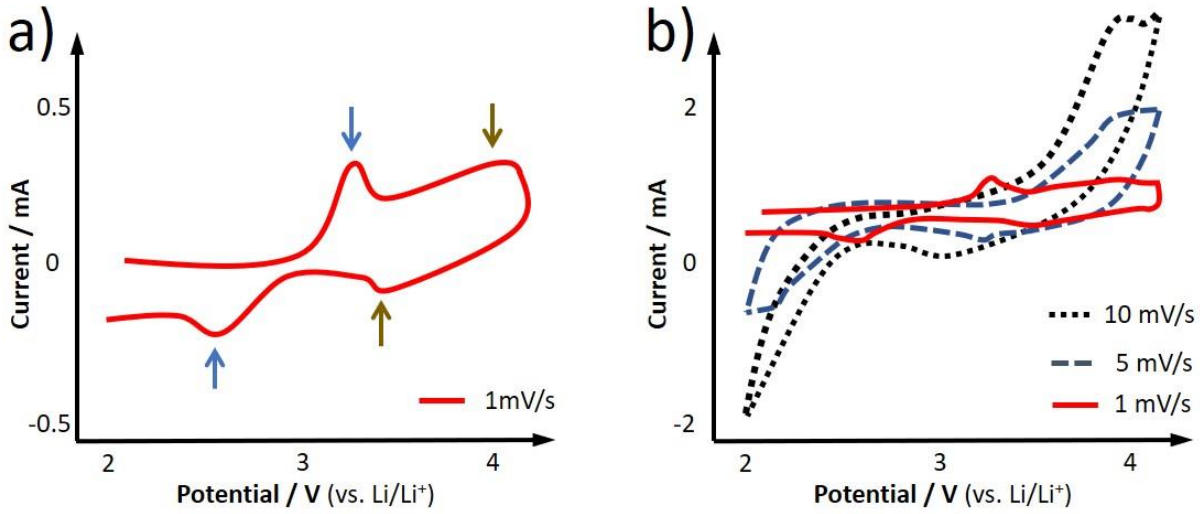

Figure 11. Schematic cyclic voltammograms of I@SWCNT at 1 mV s^{-1} (A) and at 1–10 mV s^{-1} (B) recorded in 1,3–dioxolane/dimethyl ether with a 1M lithium bis(trifluoromethanesulfonyl) supporting electrolyte.

The mechanism for lithium insertion within I@SWCNT was reported by Kato *et al.*, in 2019.[49] Utilising an organic electrolyte with a lithium source, the authors were able to reversibly insert Li^+ into the I@SWCNT material. CV measurements on the material at a scan rate of 1 mV s^{-1} revealed multiple processes, (Figure 11, A) which the authors attributed to the formation of LiI_3 and LiI atomic chains upon lithium insertion in nanotubes. These processes were lost at higher scan rates of 5 mV s^{-1}, (Figure 11, B) suggesting that the insertion process was particularly slow. This was considered evidence of Li^+ diffusion along the SWCNT channel, and not through the defects inherently present in the sidewall, which was substantiated with electrochemical impedance measurements. The capacity of the material was around 75% of the theoretical maximum based on the weight of iodine, suggesting that one in four iodine atoms was not partaking in the electrochemical processes. Two plateaus were observed in the charge-discharge experiments, in accordance with the observed CVs, and the capacity retention was high over the first few cycles. This was likely due to the iodine being held within the SWCNT and not becoming solvated by exposure to solvent in the cell. Another explanation for this, which has been used in other studies for materials inside carbon nanotubes (see Sulfur section below), is the increase in volume of the lithiated species inside the SWCNT "plugs" up the internal cavity, blocking any more lithium from reaching redox active species in the centre of the carbon nanotubes. Utilising Raman spectroscopy and diagnostic SWCNT vibrational modes, the authors reported that the formation of the reaction products could be monitored, proving that the LiI_x species and I_2 species were formed within the SWCNT cavity upon lithium insertion. Preparing a sample of CsI@SWCNT, the authors utilised Raman spectroscopy to further prove that they could extract an alkali metal from its iodide salt from within the SWCNT through electrochemical oxidation.

Table 4. Redox reactions of halogens and POMs confined within carbon nanotubes

Materials and Redox process	CNT diameter & synthesis method	Observation	Electrode	Range of potentials	Electrolyte	Ref.
$2I^- + SWCNT \rightarrow 2I_2 + SWCNT + 2e^-$	~1.5 nm SWCNTs. Arc-discharge with Y/Ni catalyst.	Applying a potential of 0.74 V vs Ag/Ag^+ drove the encapsulation of iodine from solution into the SWCNT, possibly via oxidation of surface bound iodide to iodine, followed by charge transfer from the SWCNT to the iodine, resulting in polyiodide formation and subsequent filling.	SWCNT bucky paper WE, Ag/Ag^+ RE and Pt CE.	– 0.74 to +0.74 V vs Ag/Ag^+	Aqueous 1M NaI.	45 (Song)
$3I@SWCNT + Li^+ + e^- \rightarrow LiI_3@SWCNT$ $LiI_3@SWCNT + 2Li^+ + 2e^- \rightarrow 3LiI@SWCNT$	~2.5 nm SWCNTs. Gas phase CVD method (eDIPS).	Two lithiation processes of the encapsulated iodine could be observed by cyclic voltammetry. Two corresponding plateaus were observed in the galvanostatic charge-discharge curves. The formation of different iodide species could be followed with Raman spectroscopy.	Two-electrode cell with SWCNT (bucky paper) on Cu foil WE, Li metal foil CE.	+2 to +4 V vs Li/Li^+	1M Lithium bis(trifluoromethane-sulfonyl)imide (LiTFSI) in DOL/DME (1:1 v/v)	49 (Kato)
$CsI@SWCNT \rightarrow 1/3CsI_3@SWCNT + 2/3Cs^+ + 2/3\ e^-$ $CsI_3@SWCNT \rightarrow 3I@SWCNT + Cs^+ + e^-$	~2.5 nm SWCNTs. Gas phase CVD method (eDIPS).	Similar plateau potential in the charge-discharge curve to I@SWCNT.	Two-electrode cell with SWCNT bucky paper on Cu foil WE, Li metal foil CE.	+3 to +4 V vs Li/Li^+	1M LiTFSI in DOL/DME (1:1 v/v)	49 (Kato)
$[P_2W_{18}O_{62}]^{6-}@SWCNT + 2e^- \rightarrow [P_2W_{18}O_{62}]^{8-}@SWCNT$ $[P_2W_{18}O_{62}]^{8-}@SWCNT + 2e^- + 2H^+ \rightarrow [H_2P_2W_{18}O_{62}]^{8-}@SWCNT$ $[H_2P_2W_{18}O_{62}]^{8-}@SWCNT + 2e^- + 2H^+ \rightarrow [H_4P_2W_{18}O_{62}]^{8-}@SWCNT$	~1.4 nm SWCNTs. Arc-discharge with Y/Ni catalyst.	Three reversible reductions of POM encapsulated within SWCNT were observed with a 1M H_2SO_4 electrolyte. FWHM values indicate these could have been two-electron processes. When carrying out the voltammetry with a 1M NaOH electrolyte, POM redox processes could still be observed, indicating that the SWCNTs stabilised the	Thin film of POM@SWCNT on GCE WE, saturated calomel RE, Pt wire CE.	+0.3 to – 0.7 V *vs* SCE	1M H_2SO_4 and 1M NaOH.	51 (Jordan)

		encapsulated POMs from hydrolysis.				
$[PW_{12}O_{40}]^{3-}$ @SWCNT + e^- + → $[PW_{12}O_{40}]^{4-}$ @SWCNT $[PW_{12}O_{40}]^{4-}$ @SWCNT + e^-→ $[PW_{12}O_{40}]^{5-}$ @SWCNT $[PW_{12}O_{40}]^{5-}$ @SWCNT + $2e^-$ + $2H^+$ → $[H_2PW_{12}O_{40}]^{5-}$ @SWCNT	~1.4 nm SWCNTs. Arc-discharge with Y/Ni catalyst.	Three reversible reductions of the POM encapsulated within SWCNT were observed with a 1M H_2SO_4 electrolyte. Some POM reductions were still observed with a 1M NaOH electrolyte.	Thin film of POM@SWCNT on GCE WE, saturated calomel RE, Pt wire CE.	+0.3 to – 0.7 V *vs* SCE	1M H_2SO_4 and 1M NaOH.	51 (Jordan)

Polyoxometalates

Polyoxometalates (POMs) are discrete, molecular metal oxides composed of early transition metals with d^0 and d^1 configurations with well-defined structures. Composed of multiple metal centres connected within an oxide framework, these species may undergo multiple reversible reductions. Their broad range of tuneability (both structural and compositional) stimulated has significant interest into their use as electrocatalysts and redox active components in charge storage materials.[50] Recently, our group has reported POMs confined within SWCNTs (POM@SWCNT).[51] Both the Keggin $[PW_{12}O_{40}]^{3-}$ and Wells-Dawson $[P_2W_{18}O_{62}]^{6-}$ polytungstate anions were readily encapsulated within the hydrophobic SWCNT interior, driven by the oxidation of the host-SWCNT by the guest-POMs in solution, and the subsequent coulombic force driving POM molecules into nanotube cavities (Figure 12, a-c).

CV measurements on POM@SWCNT materials in a 1M H_2SO_4 aqueous electrolyte showed that the encapsulated POM molecules could be electrochemically addressed upon encapsulation (Figure 12, d & e). The reversible redox processes demonstrated large peak currents and peak-to-peak separations of approximately 10 mV at a scan rate of 0.1 Vs^{-1}, suggesting rapid charge transfer between the macroscopic electrode and encapsulated POM, mediated by the highly conductive SWCNT and their intimate contact with the POM guest-molecules. Increasing the scan rate led to a linear increase in the peak current of all

processes, as expected for non-diffusional redox processes, and peak-to-peak values increased negligibly with increasing scan rates. When comparing the loading of the POM in POM@SWCNT structures, determined by thermal gravimetric analysis (TGA), to the charge passed during redox, it was estimated that approximately 80-90% of the encapsulated POM molecules remained electrochemically addressable. Cycling the POM@SWCNT materials over 1000 cycles demonstrated greater stability of the molecules in nanotubes during electrochemical cycling as compared to free molecules, with approximately 50% of the current retained over 1000 cycles for POM@SWCNT *versus* ~3% for POM in solution (Figure 12, f). In addition to this enhanced stability over repeated cycles, tests of the POM@SWCNT materials in 1M NaOH (conditions that normally completely hydrolyse POMs) showed faradaic current from the encapsulated POMs, suggesting that encapsulation within the SWCNT led to a significant stabilisation of the POM molecules against hydrolysis (Figure 12, g).

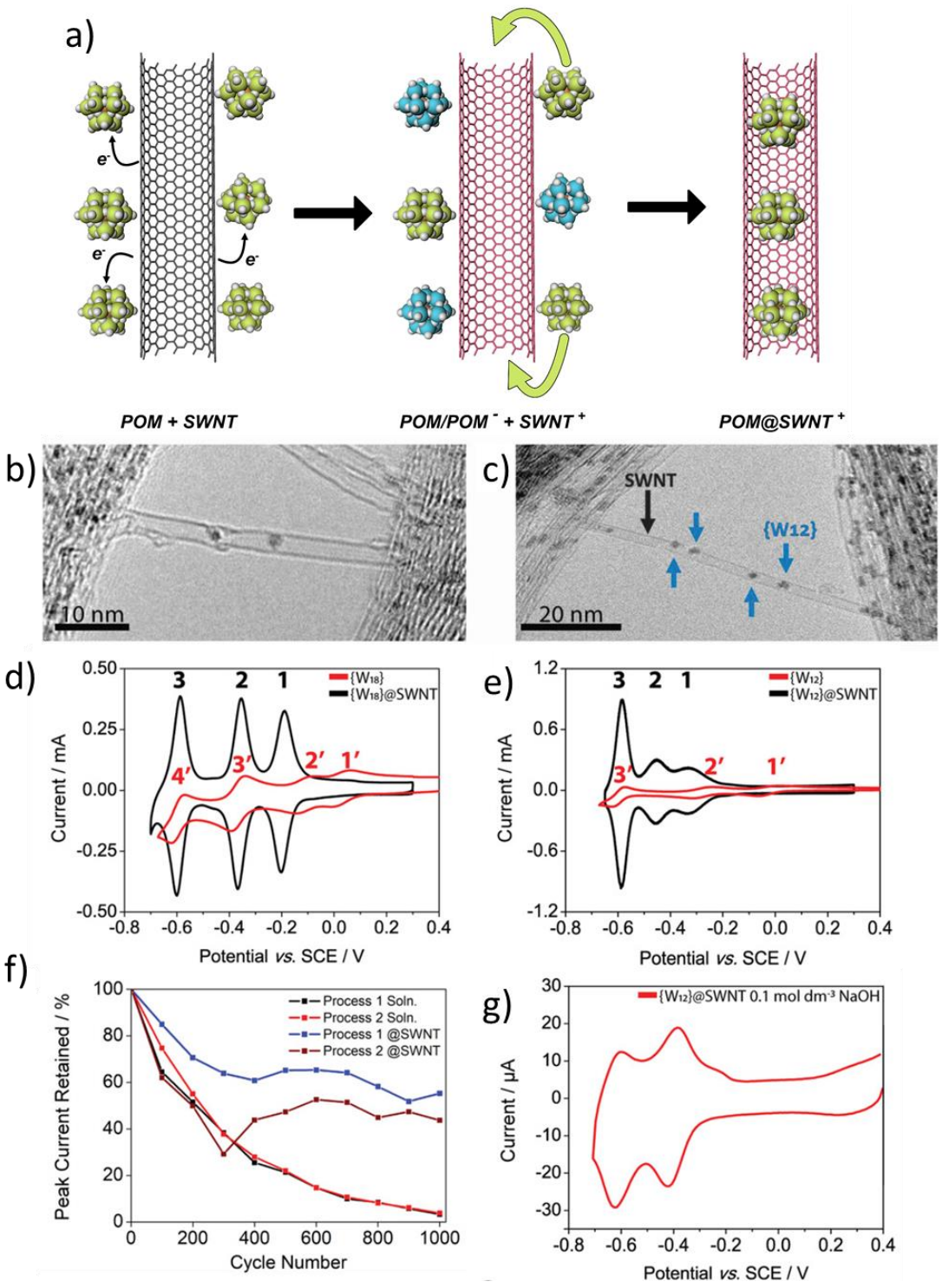

Figure 12. (a) Schematic diagram depicting the initial charge transfer between SWCNT and POM molecules in solution, leading to their encapsulation within the SWCNT. TEM images of $[P_2W_{18}O_{62}]$@SWCNT (b) and $[PW_{12}O_{40}]$@SWCNT (c). Voltammograms of $[P_2W_{18}O_{62}]$@SWCNT and $[PW_{12}O_{40}]$@SWCNT films acquired in 1M H_2SO_4 at a scan rate of 0.1 V s^{-1}, ((d) and (e) respectively, black lines, red lines show POM solution CVs). (f) Charge retained over 1000 cycles for $[P_2W_{18}O_{62}]$@SWCNT and $K_6[P_2W_{18}O_{62}]$ in solution (labelled inset) acquired in 1M H_2SO_4 at a scan rate of 0.1 V s^{-1}. (g) CV of $[PW_{12}O_{40}]$@SWCNT in 1M NaOH at a scan rate of 0.1 V s^{-1}. Figure adapted from reference 51 with permission from Wiley, copyright 2019.

Sulfur

First reported in the 1960s lithium-sulfur (Li-S) batteries have been investigated due to their extremely high specific energies (2600 W·h kg^{-1}) and the high abundance of sulfur within the earth's crust. Although the Li-ion battery has become the gold standard in recent years, sulfur presents an opportunity to greatly increase the electrification of transport and the miniaturisation of batteries.[52,53] However, issues such as low conductivity, large volume changes and high solubility of polysulfide intermediates during charge-discharge means that Li-S batteries require further optimisation, and novel types of Li-S architectures may be needed to realise Li-S widespread implementation.[54] In this context, the encapsulation of sulfur within carbon nanotubes to stabilise the intermediate soluble polysulfides and simultaneously provide a conductive support, is particularly important.

The isolation of chains of sulfur through the encapsulation within SWCNTs was reported by Fujimori *et al.*[55] in 2013 and generated a surge in interest in the applicability of sulfur redox chemistry confined within SWCNTs for energy storage. In 2015 Yang *et al.* published the first study on the lithiation of chains of sulfur confined within SWCNTs.[56] The authors showed that the capacity of sulfur@SWCNT (weight of carbon included) approached 2000 mAh g^{-1}, and with the mass of the carbon removed approached 1500 mAh g^{-1}, close to the theoretical max of sulfur (1675 mAh g^{-1}), suggesting that sulfur@SWCNT was a highly electroactive material (Figure 13). CV measurements at a scan rate of 0.1 mV s^{-1} revealed multiple redox

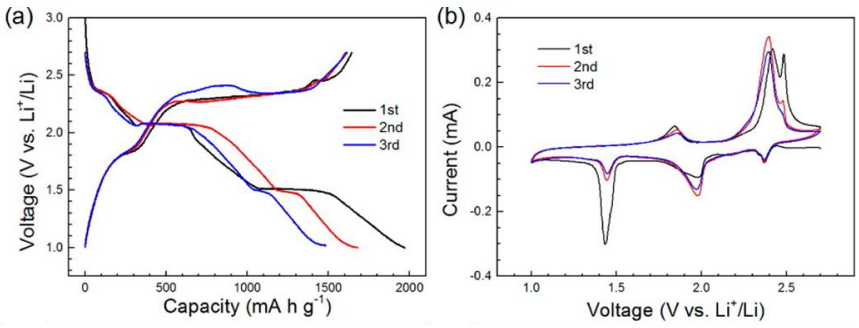

Figure 13. (a) Charge-discharge curves of S@SWCNT charged at 0.1 C (both C rate and capacitance based on the weight of S only). (b) CV measurements for S@SWCNT showing the three initial cycles at a scan rate of 0.1 mV s^{-1}. Figure adapted from reference 56 with permission from American Chemical Society, copyright 2015.

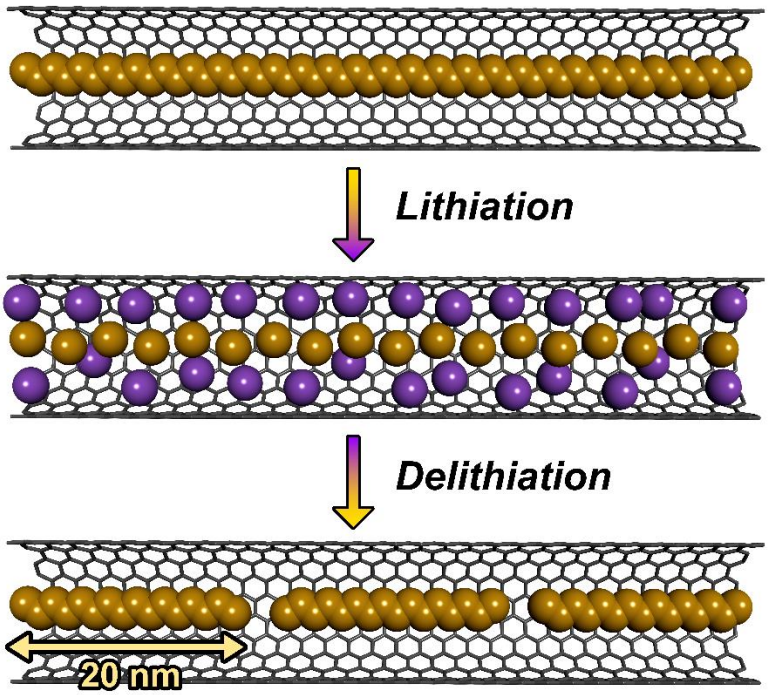

Figure 14. Scheme demonstrating the electrochemical lithiation/delithiation mechanism of sulfur chains (orange and purple circles are S and Li atoms respectively) confined within SWCNT as proposed by Yang et al. (reference 56) Lithiation of encapsulated sulfur results in a mix of Li_2S_2 and Li_2S. Delithiation results in partial reformation of sulfur chains, with lengths of around 20 nm.

processes, which were seen in the charge-discharge curves as distinct plateaus. A particularly large reduction process was observed at 1.45 V which was only observed in the linear sulfur chains confined within SWCNTs, decreasing in intensity after the first CV cycle, potentially due to structural changes in the material upon cycling, such as the formation of an SEI layer. After an initial drop in capacity, the material appeared to have a reversible capacity of around 800 mAh g^{-1} over 20 cycles. The authors noted the kinetic limitations of the system, due to the lithium diffusion along the high aspect ratio SWCNT. Utilising *ex situ* XPS measurements of the material during discharge, the authors were able to observe the reduction of the sulfur chains, initially forming Li_2S_4, then Li_2S_2 and Li_2S. The final reduction product Li_2S was observed, however at this potential Li_2S_x ($x \geq 4$) was also present which the authors attributed to the sulfur chains close to the centre of the SWCNT axis, where lithiation would be more inhibited due to less efficient mass transport of Li^+ to the centre of the SWCNTs. Utilising X-ray diffraction methods, the products of the sulfur lithiation in confinement were monitored, demonstrating that following lithiation the long linear sulfur

chains were gradually shortened, enhancing lithium transport into nanotubes in subsequent cycles, although the initial long sulfur chains were not recoverable upon delithiation (Figure 14). The evolution of diffraction peaks upon potential cycling suggests a solid phase reaction of sulfur to Li_2S, rather than the typical solid-liquid-solid mechanism, which proceeds *via* polysulfide intermediates. Raman spectroscopy measurements suggested that upon lithiation the sulfide products interacted strongly with the SWCNT sidewalls.

In 2017, Milroy *et al.* reported the fabrication of a thin film "microbattery" based on S@SWCNT using an inkjet method.[57] The authors could control the morphology of the active material on SiO_2 or aluminium foil, reporting reversible capacities of around 700 mAh g^{-1} over 100 cycles, opening up the applicability of sulfur in the miniaturisation of battery technology. UV-visible absorption spectroscopy analysis of the cycled cells found no evidence of polysulfide intermediates, corroborating that encapsulated sulfur converts to the lithium sulfide in the solid state, as proposed by Yang *et al*.[56]

In 2018, Urita *et al.* set out to prove that Li_2S_x chains were formed within SWCNT and DWCNT using electron microscopy imaging and analysis.[58] TEM imaging and electron energy loss spectroscopy (EELS) analysis of the sulfur in nanotubes before and after lithiation demonstrated that the structure of the sulfur chains was highly dependent on the diameter of the host-nanotube, with double atomic chains, single atomic chains and even S_3 fragments observed depending on the diameter of nanotube. Charge-discharge curves of the different samples gave different numbers of plateaus, as well as different CV responses, suggesting that the diameter of the host-nanotube controlled the redox chemistry for Li insertion, which becomes severely inhibited for nanotubes with a diameter below 1.4 nm. Utilising a combination of *ex situ* scanning transmission electron microscopy and electron energy loss spectroscopy (STEM-EELS), the authors mapped the location of lithium after cycling of the sulfur encapsulated nanotubes, and found that for the narrower nanotubes, lithium was not detectable in the interior space, consistent with the poorer electrochemical response (Figure 15). For the large diameter nanotubes, lithium was observed within the

interior space of the SWCNT by STEM-EELS, suggesting that the increased diameter reduced the steric hinderance on lithium transport in the nanotube, allowing lithiation to take place. This was also in good agreement with the galvanostatic charge-discharge curves. Measuring the lithium *K*-and sulfur $L_{2,3}$-edges with STEM-EELS allowed the authors to probe the local bonding environments of the redox species inside nanotubes, showing that the Li was bound to the sulfur.

An alternative point of view on lithiation of S@SWCNT was proposed by Fu *et al.* suggesting the reduced polysulfides could be stabilised *via* solvated Li^+ ions through the SWCNT side wall.[59] The authors encapsulated sulfur within SWCNT samples with an average diameter of 1.55 nm and 1 nm (written as EA-SWCNT and HiPCO-SWCNT respectively, arc-discharge and HiPCO synthesised respectively), and carried

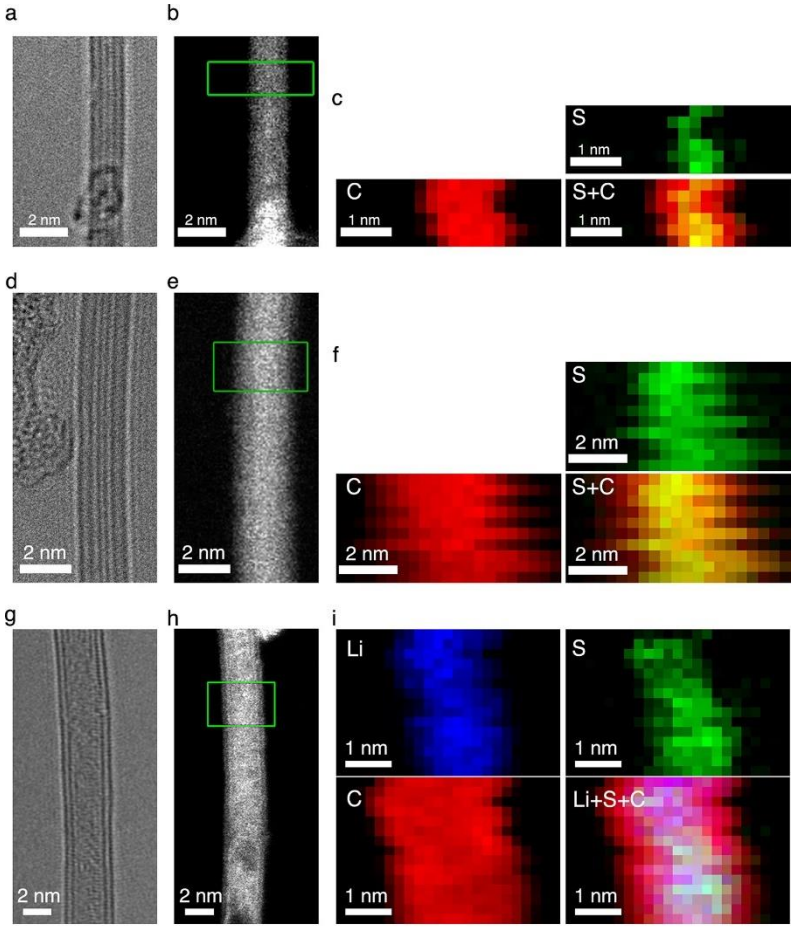

Figure 15. TEM, annular dark field (ADF) and STEM–EELS images of single S chains in DWCNT (a–c), double S chains in DWCNT (d–f) and small S species in wider DWCNT (g–i) after electrochemical cycling. Figure reproduced from reference 58 with permission from American Chemical Society, copyright 2018.

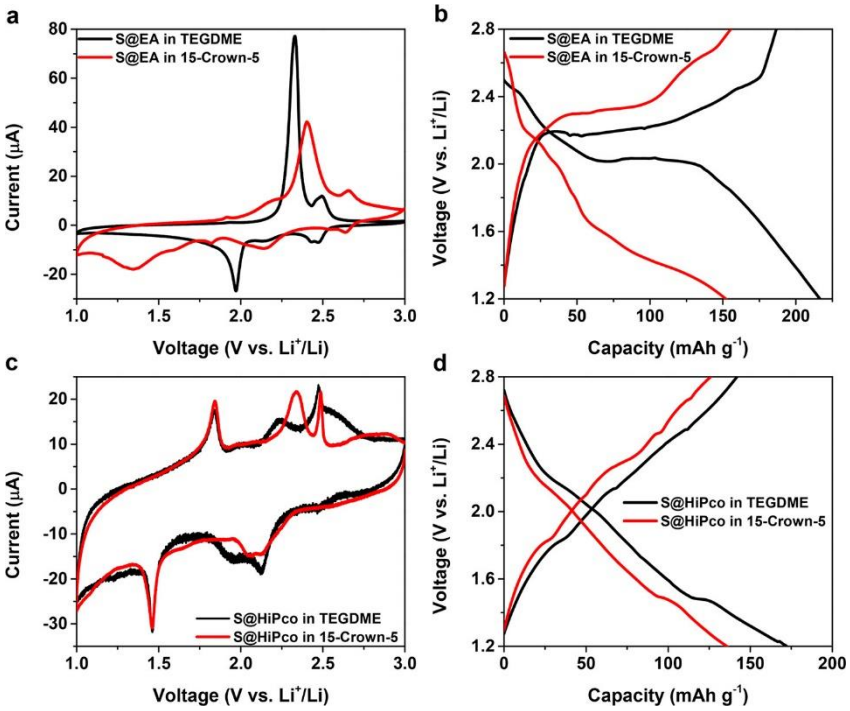

Figure 16. CV plot (a) and charge–discharge curve (b) of S@EA-SWCNT (diameter of 1.5 nm) in TEGDME and 15–crown–5. CV plot (c) and charge–discharge curve (b) of S@HiPCO-SWCNT (diameter of 1 nm) in TEGDME and 15–crown–5. CVs acquired at a scan rate of 0.05 mV s^{-1} and the charge–discharge curves acquired with a current density of 4 mA g^{-1}. Current density and capacity are with respect to the total mass (S and carbon) of the electrode material. Figure reproduced from reference 59 with permission from the American Chemical Society, copyright 2018.

out charging experiments in tetraethylene glycol dimethyl ether (TEGDME) and the equivalent crown ether (15-crown-5) with 1M lithium bis(trifluoromethane sulfonyl)imide supporting electrolyte. Utilising mass spectrometry and DFT calculations the authors were able to predict the solvent shell of Li^+ ions, demonstrating the true size of the solvated cation, with values of 10.87 Å and 11.34 Å for $[Li(TEGDME)]^+$ and $[Li(15\text{-crown-50}]^+$ respectively, at their largest dimension, aiding in understanding the mass transport of Li^+ in each solvent system. TEM analysis of S@SWCNT materials before cycling experiments showed short chains of sulfur, described as being closer to the optimal S_8 ring geometry. CVs of both S@EA-SWCNT and S@HiPCO-SWCNT materials in both solvents gave varied responses (Figure 16). In the S@EA-SWCNT material the changes in CV between the two solvents were attributed to differences in solvent viscosity, which could hinder the lithium transport to the encapsulated sulfur in the higher viscosity solvent. The charge-discharge curves of the S@EA-SWCNT nevertheless showed a distinct plateau in both solvent systems, attributed to the lithiation of sulfur within the nanotube, due to the wider diameter nanotube

being able to incorporate solvated Li^+ ions in both electrolytes. In contrast, CVs of S@HiPCO-SWCNT showed processes with smaller currents and at different potentials to S@EA-SWCNT. Changing the solvent appeared to have a lesser impact on the CV response of S@HiPCO-SWCNT, as neither solvated Li^+ ion should have been able to enter the nanotube interior. The charge-discharge curves of S@HiPCO-SWCNT did not appear to show distinct plateaus as in the wider EA-SWCNT sample, further indicating that lithiation did not occur. The overall capacities also appeared to be much lower. The authors proposed that sulfur confined within the SWCNT was reduced through the nanotube sidewall *via* an "out-of-plane π-electron interaction", with the lithium cations located outside the SWCNT (Figure 17). The authors utilised *operando* Raman spectroscopy to further clarify the nature of sulfur products formed during charge-discharge, which also suggested that lithium did not directly react with the encapsulated sulfur chains in the narrower SWCNTs during cycling. Raman results, which were in agreement with XPS measurements, showed lower amounts of Li_2S formed in S@HiPCO-SWCNT than in the wider S@EA-SWCNT after electrochemical lithiation, suggesting that lithium could not penetrate into S@SWCNT when the nanotube diameter was 1 nm.[60]

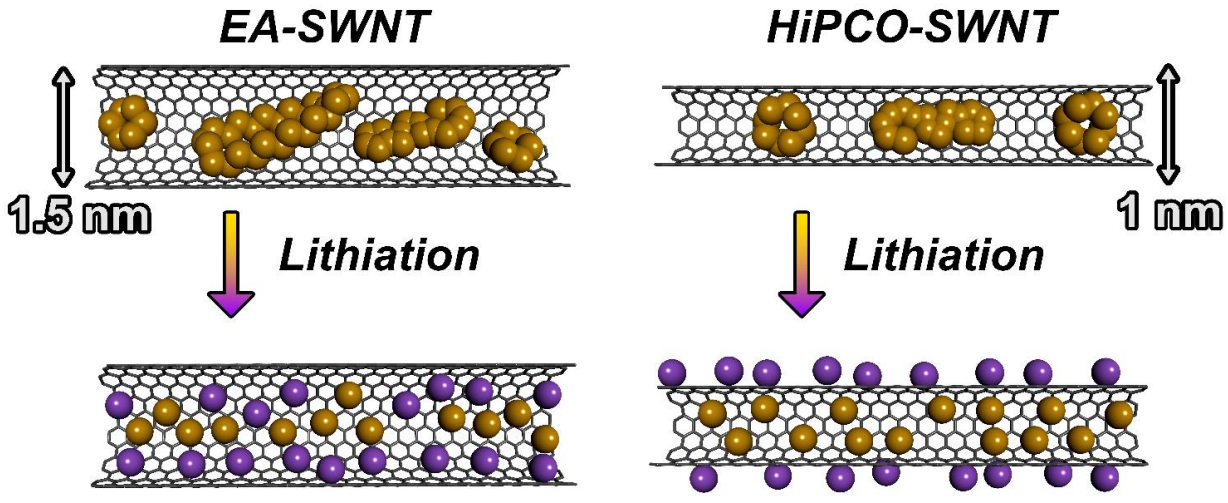

Figure 17. Scheme demonstrating the electrochemical lithiation of sulfur confined within EA-SWCNT and HiPCO-SWCNT as proposed by Fu et al. (reference 59). Confined sulfur (orange circles) is in the form of shorter, more irregular chains, closer to cyclic S_8, rather than the previously observed linear or zigzag sulfur chains (reference 55). Lithiation of S@EA-SWCNT leads to encapsulated lithium cations (purple circles) and sulfide anions, whereas lithiation of S@HiPCO-SWCNT led to S^{2-}/S_2^{2-} in nanotubes and Li^+ located on the outside of the nanotube wall, due to the smaller internal volume not accommodating Li^+.

Table 5. Redox reactions of sulfur confined within carbon nanotubes.

Redox process	CNT diameter & synthesis method	Observation	Electrode	Range of potentials	Electrolyte	Ref.
$4S_x$@CNT + $2xe^-$ + $2xLi^+ \rightarrow$ xLi_2S_4@CNT Li_2S_4@CNT + $2e^-$ + $2Li^+ \rightarrow$ $2Li_2S_2$@CNT Li_2S_2@CNT + $2e^-$ + $2Li^+ \rightarrow$ $2Li_2S$@CNT	~1 nm SWCNT/DWCNT mixture. Synthesis method not stated.	The proposed mechanisms are based on reduction products measured by XPS. The starting encapsulated S is in the form of sulfur chains. Li_2S_x ($x \geq 4$) was also seen in the final reduction product. XRD suggests a solid-phase reaction of sulfur rather than typical solid-liquid-solid.	Two-electrode Swagelok-type cell with cathode made from S@SWCNT and poly(vinyl difluoride) (PVD) 85:15, mixed as slurry in N-methyl-2-pyrrolidone (NMP) coated on Al Foil. Li foil anode.	+1.0 to +2.7 V vs Li^+/Li. CV was carried out at 0.1 mV/s.	1 M LiTFSI in 1,3-dioxolane/1,2-dimethoxymethane (DOL/DME, 1:1 v/v).	56 (Yang)
$2S_3^-$@CNT + $4e^-$ + $6Li^+ \rightarrow$ $3Li_2S_2$@CNT OR S_3^-@CNT + $5e^-$ + $6Li^+ \rightarrow$ $3Li_2S$@CNT	<1nm internal diameter DWCNTs. Derived from arc discharge SWCNTs (Ni/Y catalyst) filled with C_{60} followed by thermal decomposition to form DWCNTs ~2.5 nm SWCNTs. Produced by gas-phase CVD (eDIPS).	A solid-phase reaction is proposed (i.e no soluble polysulfides). Presence of Li in nanotube interior after lithiation is confirmed with EELS for S@SWCNT where nanotube d=1.8nm, but not where d=0.6 or 0.8 nm. Processes given are not considering possible charge compensation by nanotube.	Three-electrode Swagelok-type cell with a cathode made from S@SWCNT pressed onto Ni mesh (without binder) and Li foil on Ni mesh as RE and CE.	+1.0 to +2.7 V, with charging and discharging performed in constant current mode, with current density set to 0.1 C.	1 M LiTFSI in DOL/DME (1:1 v/v).	58 (Urita)
S_x@EA-SWCNT + $2xe^-$ + $2xLi^+$ → xLi_2S@EA-SWCNT via soluble polysulfides	~1.4 nm SWCNTs. Arc-discharge with Ni/Y catalyst.	SWCNTs are wide enough for solvated Li^+ (in both electrolytes) to enter nanotube. Electrochemical processes are affected by solvent viscosity. The final product is postulated.	Two-electrode coin cell with cathode made from 90 wt % S@EA-SWCNT and 10 wt% polyvinylpyrrolidone with Al Foil current collector and Li foil CE.	+1 to +3 V vs Li^+/Li.	1M LiTFSI in tetraethylene glycol dimethyl ether (TEGDME) and 1M LiTFSI in 1,4,7,10,13-pentaoxacyclopentadecane (15-crown-5).	59 (Fu)

S_x@HiPCO-SWCNT + $ne^- + nLi^+ \rightarrow S_x^{n-}$ @HiPCO-SWCNT/n[Li^+]	~0.9 nm SWCNTs. High pressure carbon monoxide CVD synthesis.	The HiPCO-SWCNT nanotubes are too narrow to accommodate solvated lithium ions, and reduction of the sulfur *via* out-of-plane π-electrons of carbon nanotube wall is proposed, with Li^+ located outside of the nanotube cavity.	Two-electrode coin cell with cathode made from 90 wt % S@HiPCO-SWCNT and 10 wt% polyvinylpyrrolidone with Al Foil current collector and Li foil CE.	+1 to +3 V vs Li^+/Li.	1M LiTFSI in TEGDME and 1M LiTFSI in 15-crown-5.	59 (Fu)

Conclusion

As carbon nanotubes are rapidly becoming established as highly effective containers for molecules, the level of interest in electrochemical reactions confined in carbon nanotubes begins to grow and demonstrate great opportunities for diverse redox chemistry accessible within carbon nanotubes as well as the complexity of the process. It is evident that the high conductivity of carbon nanotubes enables effective electronic communication between the guest-molecules confined within their cylindrical cavities and macroscopic electrodes, allowing large numbers of redox-active molecules to be electrochemically addressed. The stable nature of the cylindrical cavity and protection of electrochemically active guest-species by the host-nanotubes may stabilise the redox active centres during electrochemical cycling against hydrolysis and solvolysis, volumetric expansion and leaching. This in turn leads to greater stability over multiple charge-discharge cycles, potentially improving the durability of redox active materials and enhancing their use in energy storage devices.

However, the current understanding of redox processes confined within nanotubes remains insufficient, with several fundamental phenomena, including the mechanism of ion access within carbon nanotube cavities remaining poorly understood. For example, the charge conservation law demands rigorous

consideration of electrolyte ion diffusion from the surrounding solution into/onto the host-nanotube during the oxidation or reduction of confined guest-molecules, yet even basic questions, such as whether electrolyte ions may freely penetrate the nanotube interior, remain unclear, with conflicting evidence in the literature. Many studies do not discuss the role of electrolyte at all, despite a clear need for these considerations, and some works, such as the reduction of fullerenes in C_{60}@SWCNT or sulfur chains in S_x@SWCNT, lead to conclusions that are mutually exclusive.

The role of the solvent also needs clarification, particularly in context of solvation shells and nanotube-solvent interactions. A number of reports indicate significant solvent effects on the observed electrochemical response of encapsulated materials, which are interpreted as steric effects, or nanotube-solvent interactions. The importance of SEIs is mentioned in the literature as a factor leading to the desolvation of ions, allowing them to freely move between the entrance of the nanotube and the redox active molecules located deep within the nanotube cavity, although the exact nature of any SEI is often overlooked when investigating molecule@nanotube electrochemical systems, and there is a need for in-depth investigation into the composition and structure of such SEIs. Furthermore, the enthalpic and entropic driving forces for desolvation of ions in confinement may play a crucial role with carbon nanotubes, which remains largely unexplored. Overall, the this leads to a confusing landscape, with no standard protocols or best practices for accessing the redox chemistry of guest-species confined within nanotubes, and many different factors, such as solvent cage, ion-ion interactions, guest-electrolyte interactions, solvent polarity and steric barriers, are at play when electrochemical measurements on molecule@nanotube systems are carried out. This is unsurprising, considering the vast field of electrochemistry and the complex nature of host-guest materials, making the interpretation of experimental results challenging. A stronger link between nanomaterials design and electrochemical experimental approaches is therefore required to progress the understanding of these materials.

Despite these challenges, there is evidence that confinement at the nanoscale can offer significant benefits, such as improved cyclability, lowered overpotentials and materials with tuneable capacities. Future exploration of electrochemistry confined within SWCNTs and DWCNTs could help to discover new fundamental redox phenomena at the single-molecule level, as well as to advance many practical applications, including energy storage and conversion materials,[10] sensing devices and electrocatalysts.[61, 62]

Acknowledgements

We would like to thank University of Nottingham (Propulsion Futures Beacon of Excellence) and EPSRC (Established Career Fellowship for ANK, and Low-Dimensional Materials & Interfaces Doctoral Training Programme for WJVT) for funding. GNN, LRJ and DAW gratefully acknowledge the support of The Faraday Institution's LiSTAR project (EP/S003053/, FIRG014). JWJ would like to thank the EPSRC 2020 Doctoral Prize (EP/T517902/1). We would like to thank Prof. Y. Ishii and Prof. S. Kawasaki for assistance in preparation of figures 10 b-e, and 11.

Author Contributions

JWJ and WJVT collated the literature. All authors contributed to the writing of the manuscript.

References

1. L. Sun, X. Wang, Y. Wang and Q. Zhang, *Carbon*, 2017, **122**, 462-474.
2. M. Monthioux, *Carbon*, 2002, **40**, 1809-1823.
3. A. B. Grommet, M. Feller and R. Klajn, *Nat. Nanotechnol.*, 2020, **15**, 256-271.
4. S. A. Miners, G. A. Rance and A. N. Khlobystov, *Chem. Soc. Rev.*, 2016, **45**, 4727-4746.
5. M. V. Kharlamova, *Prog. Mater. Sci.*, 2016, **77**, 125-211.
6. V. Augustyn and Y. Gogotsi, *Joule*, 2017, **1**, 443-452.
7. S. Fleischmann, M. A. Spencer and V. Augustyn, *Chem. Mater.*, 2020, **32**, 3325-3334.
8. X. Han, Q. Gao, Z. Yan, M. Ji, C. Long and H. Zhu, *Nanoscale*, 2021, **13**, 1515-1528.
9. A. N. Khlobystov, D. A. Britz and G. A. D. Briggs, *Accounts Chem. Res.*, 2005, **38**, 901-909.
10. H. Tabassum, A. Mahmood, B. Zhu, Z. Liang, R. Zhong, S. Guo and R. Zou, *Energy Environ. Sci.*, 2019, **12**, 2924-2956.
11. B. W. Smith, M. Monthioux and D. E. Luzzi, *Nature*, 1998, **396**, 323-324.
12. L. Kavan, L. Dunsch and H. Kataura, *Chem. Phys. Lett.*, 2002, **361**, 79-85.
13. T. Pichler, H. Kuzmany, H. Kataura and Y. Achiba, *Phys. Rev. Lett.*, 2001, **87**, 267401.

14. L. Kavan, L. Dunsch, H. Kataura, A. Oshiyama, M. Otani and S. Okada, *J. Phys. Chem. B*, 2003, **107**, 7666-7675.
15. L. Kavan, L. Dunsch and H. Kataura, *Carbon*, 2004, **42**, 1011-1019.
16. N. Sun, L. Guan, Z. Shi, Z. Zhu, N. Li, M. Li and Z. Gu, *Electrochem. Commun.*, 2005, **7**, 1148-1152.
17. E. Laviron, *J. Electroanal. Chem. Inter. Electrochem.*, 1979, **100**, 263-270.
18. J. Mittal, M. Monthioux, H. Allouche and O. Stephan, *Chem. Phys. Lett.*, 2001, **339**, 311-318.
19. B. S. Krumgalz, *Journal of the Chemical Society, Faraday Transactions 1: Physical Chemistry in Condensed Phases*, 1982, **78**, 437-449.
20. M. Della Monica and L. Senatore, *J. Phys. Chem.*, 1970, **74**, 205-207.
21. K. Wu, H. Qiu, J. Hu, N. Sun, Z. Zhu, M. Li and Z. Shi, *Carbon*, 2012, **50**, 4401-4408.
22. S. Kawasaki, Y. Iwai and M. Hirose, *Mater. Res. Bull.*, 2009, **44**, 415-417.
23. T. Matsushita, Y. Ishii and S. Kawasaki, *Mater. Express*, 2013, **3**, 30-36.
24. J.-X. Li, Y. Zhao and L.-H. Guan, *Electrochem. Commun.*, 2010, **12**, 592-595.
25. X. X. Wang, J. N. Wang, H. Chang and Y. F. Zhang, *Adv. Funct. Mater.*, 2007, **17**, 3613-3618.
26. H. Shimoda, B. Gao, X. P. Tang, A. Kleinhammes, L. Fleming, Y. Wu and O. Zhou, *Phys. Rev. Lett.*, 2001, **88**, 015502.
27. L. Guan, Z. Shi, M. Li and Z. Gu, *Carbon*, 2005, **43**, 2780-2785.
28. H. Qiu, N. Sun, M. Li, Z. Shi, J. Qiu, Z. Gu and J. Yang, *J. Nanosci. Nanotechnol.*, 2011, **11**, 4034-4038.
29. N. Sun, L. Guan, Z. Shi, N. Li, Z. Gu, Z. Zhu, M. Li and Y. Shao, *Anal. Chem.*, 2006, **78**, 6050-6057.
30. A. s. S. Claye, J. E. Fischer, C. B. Huffman, A. G. Rinzler and R. E. Smalley, *J. Electrochem. Soc.*, 2000, **147**, 2845.
31. H. Cheng, H. Qiu, Z. Zhu, M. Li and Z. Shi, *Electrochimica Acta*, 2012, **63**, 83-88.
32. H. Cheng, L. Guan, Z. Shi, Z. Zhu, Z. Gu and M. Li, *Electroanalysis*, 2013, **25**, 2041-2044.
33. R. L. McSweeney, T. W. Chamberlain, M. Baldoni, M. A. Lebedeva, E. S. Davies, E. Besley and A. N. Khlobystov, *Chem. - Eur. J.*, 2016, **22**, 13540-13549.
34. L.-J. Li, A. N. Khlobystov, J. G. Wiltshire, G. A. D. Briggs and R. J. Nicholas, *Nat. Mater.*, 2005, **4**, 481-485.
35. A. Al-zubaidi, T. Inoue, T. Matsushita, Y. Ishii, T. Hashimoto and S. Kawasaki, *J. Phys. Chem. C*, 2012, **116**, 7681-7686.
36. J. Sworakowski, *Synth. Met.*, 2018, **235**, 125-130.
37. Y. Iizumi, H. Suzuki, M. Tange and T. Okazaki, *Nanoscale*, 2014, **6**, 13910-13914.
38. R. L. McSweeney, T. W. Chamberlain, E. S. Davies and A. N. Khlobystov, *Chem. Commun.*, 2014, **50**, 14338-14340.
39. S. Kawasaki, Y. Iwai and M. Hirose, *Carbon*, 2009, **47**, 1081-1086.
40. Y. Ishii, K. Tashiro, K. Hosoe, A. Al-zubaidi and S. Kawasaki, *Phys. Chem. Chem. Phys.*, 2016, **18**, 10411-10418.
41. C. Li, Y. Ishii, S. Inayama and S. Kawasaki, *Nanotechnology*, 2017, **28**, 355401.
42. T. Tsuzuki, S. Ogata and M. Uranagase, *Comput. Mater. Sci.*, 2020, **171**, 109281.
43. C. Li, Y. Ishii and S. Kawasaki, *Jpn. J. Appl. Phys.*, 2018, **58**, SAAE02.
44. C. Zhong, Y. Deng, W. Hu, J. Qiao, L. Zhang and J. Zhang, *Chem. Soc. Rev.*, 2015, **44**, 7484-7539.
45. H. Song, Y. Ishii, A. Al-zubaidi, T. Sakai and S. Kawasaki, *Phys. Chem. Chem. Phys.*, 2013, **15**, 5767-5770.
46. Y. Yoshida, Y. Ishii, N. Kato, C. Li and S. Kawasaki, *J. Phys. Chem. C*, 2016, **120**, 20454-20461.
47. Y. Taniguchi, Y. Ishii, A. Al-Zubaidi and S. Kawasaki, *J. Nanosci. Nanotechnol.*, 2017, **17**, 1901-1907.
48. C. Li, Y. Yoshida, R. Date, K. Matsushita, Y. Ishii and S. Kawasaki, *Mater. Express*, 2018, **8**, 555-561.

49. N. Kato, Y. Ishii, Y. Yoshida, Y. Sakamoto, K. Matsushita, M. Takahashi, R. Date and S. Kawasaki, *ACS Omega*, 2019, **4**, 2547-2553.
50. N. I. Gumerova and A. Rompel, *Nat. Rev. Chem*, 2018, **2**, 0112.
51. J. W. Jordan, G. A. Lowe, R. L. McSweeney, C. T. Stoppiello, R. W. Lodge, S. T. Skowron, J. Biskupek, G. A. Rance, et al., *Adv. Mater.*, 2019, **31**, 1904182.
52. M. Zhao, B.-Q. Li, X.-Q. Zhang, J.-Q. Huang and Q. Zhang, *ACS Cent. Sci.*, 2020, **6**, 1095-1104.
53. P. G. Bruce, S. A. Freunberger, L. J. Hardwick and J.-M. Tarascon, *Nat Mater*, 2012, **11**, 19-29.
54. S. S. Zhang, *J. Power Sources*, 2013, **231**, 153-162.
55. T. Fujimori, A. Morelos-Gómez, Z. Zhu, H. Muramatsu, R. Futamura, K. Urita, M. Terrones, T. Hayashi, et al., *Nat. Commun.*, 2013, **4**, 2162.
56. C.-P. Yang, Y.-X. Yin, Y.-G. Guo and L.-J. Wan, *J. Am. Chem. Soc.*, 2015, **137**, 2215-2218.
57. C. A. Milroy, S. Jang, T. Fujimori, A. Dodabalapur and A. Manthiram, *Small*, 2017, **13**, 1603786.
58. K. Urita, T. Fujimori, H. Notohara and I. Moriguchi, *ACS Applied Energy Materials*, 2018, **1**, 807-813.
59. C. Fu, M. B. Oviedo, Y. Zhu, A. von Wald Cresce, K. Xu, G. Li, M. E. Itkis, R. C. Haddon, et al., *ACS Nano*, 2018, **12**, 9775-9784.
60. T. Cui, J. Dong, X. Pan, T. Yu, Q. Fu and X. Bao, *Journal of Energy Chemistry*, 2019, **28**, 123-127.
61. M. del Carmen Gimenez-Lopez, A. Kurtoglu, D. A. Walsh and A. N. Khlobystov, *Adv. Mater.*, 2016, **28**, 9103-9108.
62. M. Aygün, M. Guillen-Soler, J. M. Vila-Fungueiriño, A. Kurtoglu, T. Chamberlain, A. Khlobystov and M. d. C. Gimenez Lopez, *ChemSusChem*, **doi: 10.1002/cssc.202101236**.